



RESEARCH ARTICLE

10.1029/2021GC010125

Key Points:

- We geochemically characterize calcite veins in normal faults that offset Cretaceous turbidites
- These veins record hydraulic fracturing and precipitation after rupturing of a reservoir, following exhumation near the new plate boundary
- The U-Pb age of the veins together with other results constrains a mid-Oligocene timing of subduction initiation at the Hikurangi margin

Supporting Information:

Supporting Information may be found in the online version of this article.

Correspondence to:

S. H. A. van de Lagemaat,
s.h.a.vandelagemaat@uu.nl

Citation:

van de Lagemaat, S. H. A., Mering, J. A., & Kamp, P. J. J. (2022). Geochemistry of syntectonic carbonate veins within Late Cretaceous turbidites, Hikurangi Margin (New Zealand): Implications for a mid-Oligocene age of subduction initiation. *Geochemistry, Geophysics, Geosystems*, 23, e2021GC010125. <https://doi.org/10.1029/2021GC010125>

Received 30 AUG 2021

Accepted 22 APR 2022

Author Contributions:

Conceptualization: Suzanna H. A. van de Lagemaat, Peter J. J. Kamp

Data curation: John A. Mering

Formal analysis: John A. Mering, Peter J. J. Kamp

Funding acquisition: Peter J. J. Kamp

Investigation: Suzanna H. A. van de Lagemaat

Methodology: Suzanna H. A. van de Lagemaat, John A. Mering, Peter J. J. Kamp

Project Administration: Peter J. J. Kamp

© 2022. The Authors.

This is an open access article under the terms of the [Creative Commons Attribution License](https://creativecommons.org/licenses/by/4.0/), which permits use, distribution and reproduction in any medium, provided the original work is properly cited.

Geochemistry of Syntectonic Carbonate Veins Within Late Cretaceous Turbidites, Hikurangi Margin (New Zealand): Implications for a Mid-Oligocene Age of Subduction Initiation

Suzanna H. A. van de Lagemaat^{1,2} , John A. Mering², and Peter J. J. Kamp²

¹Department of Earth Sciences, Utrecht University, Utrecht, The Netherlands, ²School of Science, University of Waikato, Hamilton, New Zealand

Abstract We document the geochemistry of calcite veins in the Late Cretaceous Tikiore Formation (Raukumara Peninsula, New Zealand) to characterize their fluid composition and source and to help establish the age of subduction initiation at the Hikurangi margin of the Australia-Pacific plate boundary. The calcite veins occur within normal faults offsetting turbidites that accumulated in a lower slope basin. Vein calcite trace metal content and rare earth element patterns are consistent with a seawater-derived brine composition. Oxygen isotope ($\delta^{18}\text{O}$) values range from -6.1 to $+8.4\text{‰}$ and are -0.2‰ VPDB on average; positive $\delta^{13}\text{C}$ values of up to $+28\text{‰}$ VDPB reflect methanogenesis. Oxygen isotope temperature data indicate that calcite vein mineralization occurred at temperatures in the range of 29°C – 48°C . This is markedly less than the maximum burial temperature experienced by the host rocks, which we estimate to be $104 \pm 10^{\circ}\text{C}$ at 30 – 27 Ma from the inverse modeling of apatite fission track data. The vein calcite has a 28.5 ± 4.9 Ma U-Pb age. From these data, we infer that the succession above Tikiore Formation was removed by slumping, thereby resulting in fluid overpressure in the reservoir, followed by hydraulic fracturing and the precipitation of the vein calcite. Ultimately, the data presented here from the Tikiore veins are consistent with subduction initiation at 30 – 27 Ma, based on the U-Pb age of the vein calcite and modeling of apatite fission track data for the host sandstone, corroborated by the 30 – 27 Ma timing of back thrusting on the Taranaki Fault and related foredeep development in eastern Taranaki Basin.

Plain Language Summary Subduction zones, where, most commonly, an oceanic plate turns down below an overriding continental plate, are among the most dynamic geological settings on Earth. In the frontal part of these zones, known as the forearc region, marine water along with sediments can be transported down the interface of the two plates. One water pathway can be upward into the overriding plate, where it may be trapped in fluid reservoirs. Tectonic processes ultimately fracture these reservoirs, leading to fluids being pumped along these fractures resulting in minerals being precipitated within them. In this study, we analyze the chemistry of a set of calcite veins collected from fracture zones in a sedimentary formation (Tikiore Formation) in the forearc region (Hikurangi margin) of New Zealand. We establish that the fluid source of the veins is indeed marine waters and that they precipitated at relatively cool temperatures (29°C – 48°C). Uranium-lead dating of vein calcite sample material establishes that it was precipitated 28.5 ± 4.9 million years ago. From these data and supporting geological information, we interpret the subduction zone along the Hikurangi margin, which is part of the Australia-Pacific plate boundary zone through New Zealand, to have started during the interval of 30 – 27 Ma.

1. Introduction

The Hikurangi subduction zone is the sector of the modern Australia-Pacific plate boundary east of North Island and northernmost South Island (New Zealand), where the oceanic Pacific Plate subducts beneath the continental Australia Plate (Figure 1). Early studies concluded that the modern plate boundary including the Alpine Fault sector in South Island formed at about 23 Ma (Oligocene-Miocene boundary) (e.g., Carter & Norris, 1976; Cooper et al., 1987; Field et al., 1997; Kamp, 1986). This age is based on geologic features, such as a stratigraphic change from carbonate to terrigenous sedimentation in Oligocene-Miocene sedimentary basins in New Zealand (e.g., Ballance, 1993; Carter & Norris, 1976; Field et al., 1997; Nelson & Hume, 1977), and the early Miocene start of arc volcanism in northern North Island (e.g., Ballance, 1976; Ballance et al., 1985; Hayward et al., 2001; Isaac et al., 1994). These manifestations are, however, likely to provide minimum estimates of the

Visualization: Suzanna H. A. van de Lagemaat, John A. Mering
Writing – original draft: Suzanna H. A. van de Lagemaat, John A. Mering, Peter J. J. Kamp
Writing – review & editing: Suzanna H. A. van de Lagemaat, John A. Mering, Peter J. J. Kamp

timing of initiation of the current plate boundary because substantial rock uplift is required for a wholesale change from carbonate to terrigenous sediment input to basins, and a considerable distance of subduction is needed before arc magma is typically generated. More recently, Furlong and Kamp (2013) showed from analysis of plate motions coupled with analysis of the stratigraphy in multiple basins across New Zealand that crustal extension transitioned to crustal shortening between 29 Ma at the latitude of the northern Hikurangi margin and 26 Ma in the more southerly Fordland region of southwestern South Island. This suggests that initial subduction at the Hikurangi Margin might have started at about 29 Ma but no geological confirmation of this has yet been demonstrated.

Subduction initiation at the Hikurangi Margin has previously been associated with emplacement of the East Coast Allochthon (ECA) (Brothers & Delaloye, 1982; Rait et al., 1991). The ECA is a widespread allochthon exposed in Raukumara Peninsula in eastern North Island within the forearc region of the Hikurangi margin (Figures 1 and 2). It comprises several thrust sheets of sedimentary rocks and one sheet of ocean floor lavas and is considered to have been gravitationally emplaced from offshore northeast of Raukumara Peninsula to the southwest during the latest Oligocene and earliest Miocene and into an inboard position on the Australia Plate within the principal forearc basin (Mazengarb & Speden, 2000; Rait, 1992; Stoneley, 1968). To better constrain the timing of subduction initiation at the Hikurangi margin, we report the results of geochemical analysis and U-Pb dating of calcite veins sampled from Tikihore Formation, the lowermost sedimentary formation in the ECA, exposed at Waihou Bay at the northern end of the Raukumara Peninsula (Figures 2 and 3). We then compare our geological results with predictions from plate tectonic analysis (Furlong & Kamp, 2013) about the timing of subduction initiation at the Hikurangi margin.

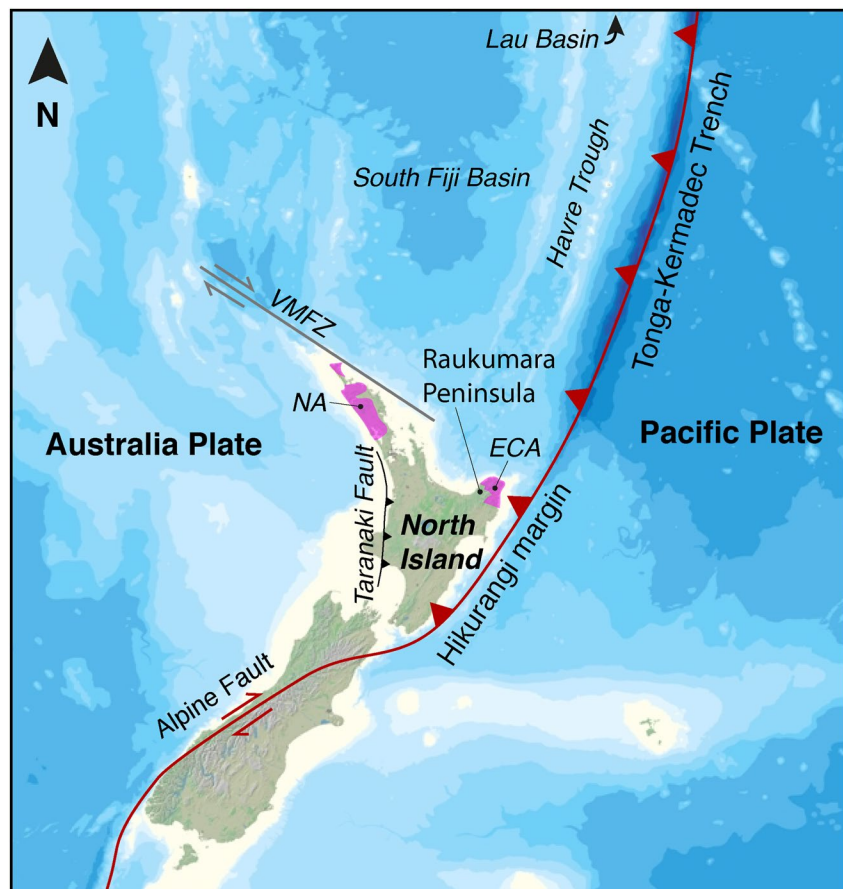


Figure 1. Tectonic Map of the New Zealand region showing the Tonga-Kermadec arc-trench system, which passes south to the ocean-continent Hikurangi margin along eastern North Island, both part of the Australia-Pacific plate boundary. Note the general distribution in pink of the Northland Allochthon (NA) and the East Coast Allochthon (ECA), and the location of the Vening Meinesz Fracture Zone (VMFZ). Background image obtained from NIWA (CANZ, 2008).

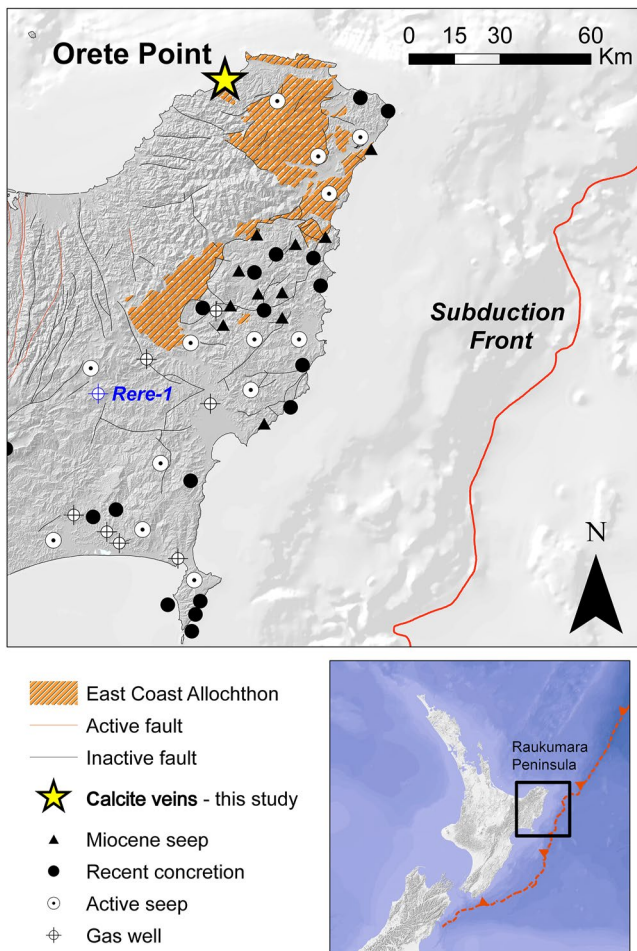
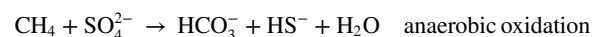


Figure 2. Raukumara Peninsula in Eastern North Island, New Zealand, in relation to the modern subduction front of the Hikurangi margin. Note the distribution of the East Coast Allochthon. Orete Point is the location of this study. The distribution of Miocene cold seep carbonate occurrences and active seeps and springs in the northern part of the Hikurangi margin are also shown (from Nyman et al., 2010).

Our approach to analysis and interpretation of the carbonate veins in the Tiki-hore Formation follows that of prior studies of syntectonic vein carbonates and fluid flow through accretionary margins within the Cascadia Margin (e.g., Ritger et al., 1987; Sample et al., 1993), the Californian Margin (Campbell et al., 2002), and the Nankai Trough (e.g., Sakai et al., 1992; Sample et al., 2017). We also draw upon a body of work on the chemistry of active fluid seeps within the Hikurangi Margin (Figure 1), including saline springs on land (e.g., Barnes et al., 2019; Giggenbach et al., 1995) and cold seeps at sites offshore (Lewis & Marshall, 1996). In addition, we draw upon published work on fossil seafloor cold seep limestone formed atop fluid vents that were buried by ongoing Miocene and Pliocene sedimentation within the East Coast forearc basin (Campbell et al., 2008; Nelson et al., 2019; Nyman & Nelson, 2011; Nyman et al., 2010).

The precipitation of carbonate in accretionary and other settings involves dissolved carbon species (e.g., CH_4 and CO_2) and cations (e.g., Ca^{2+} , Mg^{2+} , and Fe^{2+}) (e.g., Campbell et al., 2002, 2008; Sample, 1996; Vrolijk & Shepard, 1991). Rapid burial in accretionary wedges traps pore water and organic matter, which later contributes to the fluids from which vein calcite precipitates (Farsang et al., 2021). Oxidation of organic matter generates CO_2 , whereas reduction generates CH_4 (e.g., Campbell et al., 2008; Saffer, 2007). For mineralization to take place, fluid must reach and exceed carbonate saturation. Where fluid pressure exceeds lithostatic pressure at depth in a rock succession, hydraulic fracturing can result, possibly associated with a change in the stress regime (Barker et al., 2006; Beach, 1980; Brown et al., 1994; Oliver & Bons, 2001; Saffer, 2007). Fluid pulsing through fractures can cause CO_2 degassing, which increases pH and enables carbonate precipitation (Uysal et al., 2011). In methane-rich fluids, anaerobic oxidation of methane (AOM), associated with sulfate reduction, can also lead to an increase in alkalinity, enabling carbonate formation (Loyd et al., 2016):



AOM-style carbonate mineralization has been widely documented within Miocene cold seep carbonates in the eastern Raukumara Peninsula (Campbell et al., 2008; Nelson et al., 2019), in tubular concretions within a late Miocene succession resulting from fluid migration tens of meters beneath the contemporary seafloor (Nyman et al., 2010), and in Late Cretaceous

concretions (Kiel et al., 2013). There are numerous examples of modern gas seeps and saline springs on land and offshore Raukumara Peninsula, conveying aqueous fluids and dissolved gases to the surface (Barnes et al., 2019; Francis, 1995; Nyman et al., 2010).

We describe the field relations, texture, major element and trace metal composition, and stable-isotope composition of vein samples in Tiki-hore Formation to reconstruct the composition and temperature of the fluid reservoir from which the veins formed. We utilize U-Pb dating to quantitatively constrain the timing of vein carbonate mineralization. In addition, we apply apatite fission track and vitrinite reflectance methods to the vein host sandstone to constrain the thermal history of the Tiki-hore Formation. Together with the carbonate vein information, this enables us to reconstruct the sequence of events that led to the formation of the calcite veins and to interpret the timing of subduction initiation at the Hikurangi margin.

2. Tectonic and Geological Settings

The East Coast region of North Island lies inboard of the Hikurangi Trough (trench) and currently has a NE-SW trend (Figure 1). Prior to the early Miocene, its orientation was NW-SE, colinear with the east coast of Northland (e.g., Bradshaw, 1989; King, 2000). The sedimentary basement underlying this whole margin is formed by

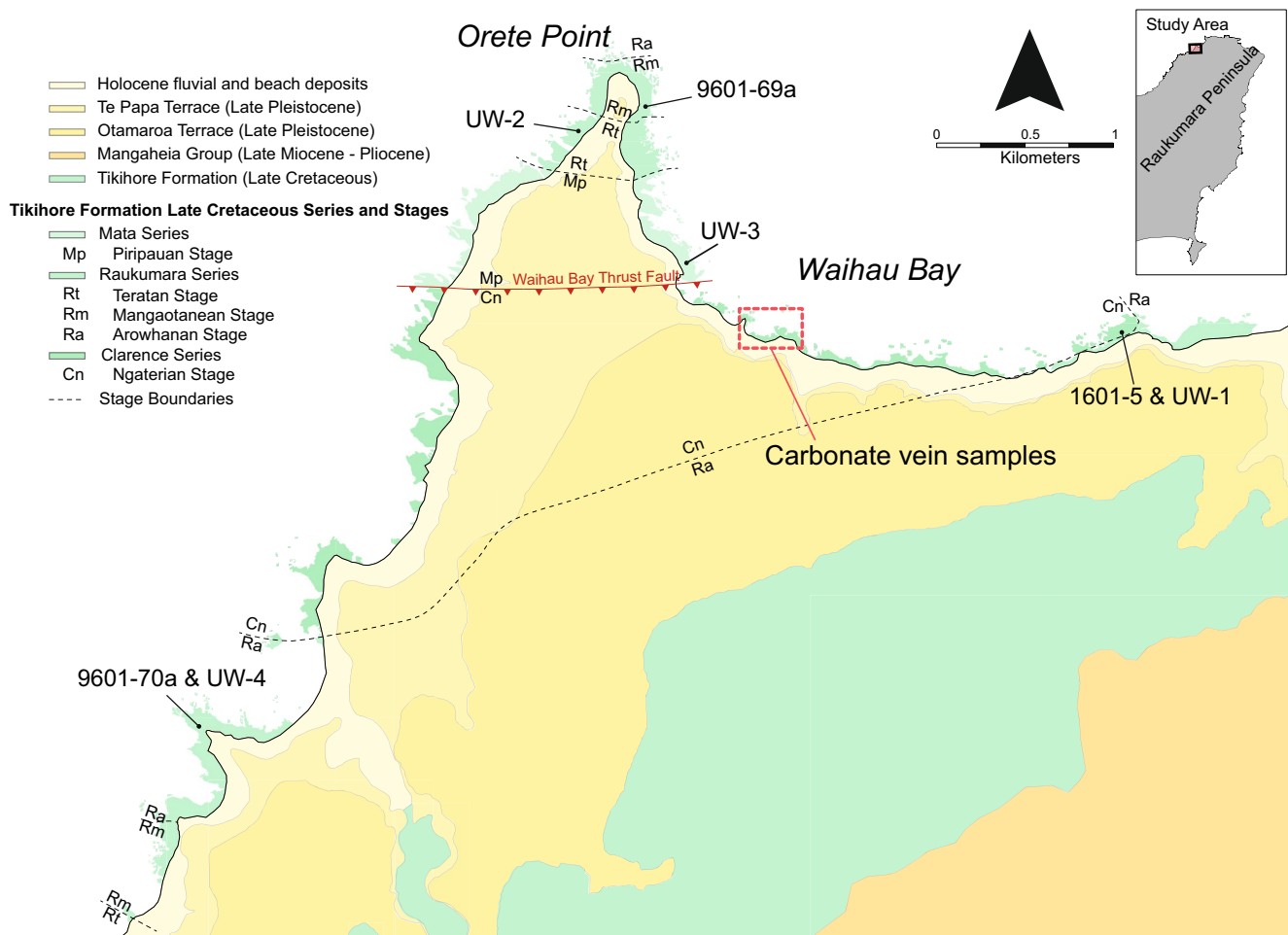


Figure 3. Geological map showing the calcite vein locations and the distribution of Tikihore Formation, including its rocky shore platform outcrop, northern Raukumara Peninsula. The distribution of New Zealand Late Cretaceous stages within Tikihore Formation and the fission track and vitrinite reflectance sample locations are also shown.

subduction accretion processes during the Cretaceous (Mazengarb & Harris, 1994). During the latest Cretaceous to Oligocene, this margin accumulated a passive margin sedimentary drape of mainly terrigenous siltstone (Tinui, Mangatu, and Ruatoria groups; Figure 4). Since the early Miocene, the part of the East Coast of North Island south of Raukumara Peninsula has been tectonically rotated clockwise to be now oriented NE-SW as demonstrated by analysis of paleomagnetic data (Lamb, 2011; Rowan et al., 2005; Walcott et al., 1981). Prior to the start of this rotation, the Australia-Pacific plate boundary developed along the eastern Northland (northern North Island) continental margin possibly as a transform fault, part of which still exists, known as the Vening Meinesz Fracture Zone (VMFZ) (Figure 1).

Two very large allochthons, the Northland Allochthon and the East Coast Allochthon (ECA; Figure 1), were emplaced onto the Australia Plate from the vicinity of the new Hikurangi Subduction Zone during the latest Oligocene and early Miocene (Ballance & Spörli, 1979; Field et al., 1997; Isaac et al., 1994; Mazengarb & Speden, 2000; Rait, 1992). Both the Northland and East Coast allochthons have similar stratigraphy, lithology, and structure, reflecting mobilization of the same Late Cretaceous and Paleogene passive margin sedimentary succession and seafloor basalt. Our study is exclusively focused on Tikihore Formation at Waihou Bay, which occurs within the ECA.

Stoneley (1968) first mapped (part of) the ECA and inferred its emplacement by gravitational sliding to the south-southwest off a structural high located offshore to the northeast of Raukumara Peninsula. Subsequent mapping has established the full extent of the ECA (Figure 2; Rait, 1992; Mazengarb & Speden, 2000) and

confirmed its south-southwestward direction of emplacement as a series of gravitationally driven thrust sheets (Rait, 1992). The final phase of emplacement of the ECA into the East Coast forearc basin was accompanied by supra-allochthon accumulation of early Miocene bathyal mudstone in piggy-back basins on some of the thrust sheets (Mazengarb & Speden, 2000).

The Tikhore Formation comprises the oldest sedimentary rocks that were incorporated into the ECA and was deposited during the late Cenomanian–early mid-Santonian (c. 96–83 Ma (Crampton, 1996); upper Ngaterian–Piripauan stages of the New Zealand geological time scale; Raine et al., 2015). The Tikhore Formation is inferred to have accumulated within an accretionary slope basin atop the outer edge of the Cretaceous accretionary wedge (Mazengarb & Harris, 1994), known as the Torlesse Complex (Edbrooke et al., 2015; Mortimer, 2004). The Tikhore Formation is one of several units within the Ruatoria Group (Figure 4), which includes all accretionary shelf and slope basin units within the ECA (Mazengarb & Speden, 2000).

The Tikhore Formation comprises mainly mass-emplaced terrigenous sandstone (turbidites) and associated hemipelagic mudstone beds. This succession is continuously exposed on the shore platform around Orete Point and part of Waihou Bay (Mazengarb & Speden, 2000) (Figures 2 and 3). The beds dip moderately to steeply and are mostly overturned. The Waihou Bay Thrust Fault (Figure 3) is a steeply dipping late reverse fault that signif-

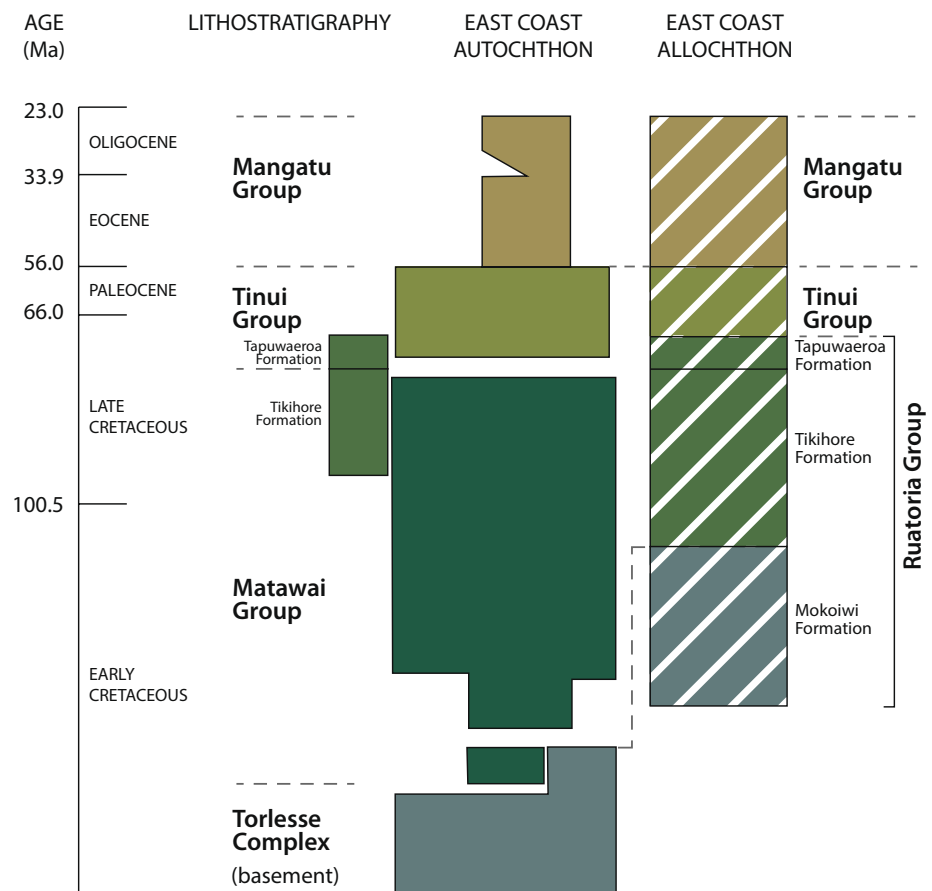


Figure 4. Stratigraphic legend for Cretaceous–Oligocene strata in the East Coast of North Island (New Zealand), following the geological mapping by Mazengarb and Speden (2000). The similar succession of lithologies for both the autochthonous and allochthonous strata reflects the late Oligocene and early Miocene emplacement of the East Coast Allochthon to the southwest and inboard of its former lower slope position on the Australia Plate continental margin. The Mokoikiwi Formation is the youngest and most outboard part of the Cretaceous accretionary wedge, now displaced inboard as part of the East Coast Allochthon; the Torlesse Complex is an older part of the same wedge. Tikhore Formation has been mapped both in the autochthon and allochthon although having differences in their duration of sediment accumulation. The calcite veins characterized in this study were collected from allochthonous Tikhore Formation at Waihou Bay.

icantly offsets the succession and juxtaposes beds of Ngaterian age (99.5–95.2 Ma) against beds of Piripauan age (86.5–83.6 Ma) (Crampton, 1996). Otherwise, the beds are offset by normal faults with up to a few meters of displacement and by subsequent bedding-parallel thrust faults with tens of meters of offset. In a few instances, thrust faults demonstrably offset normal faults.

3. Analytical Methodology

3.1. Petrographic Observations

Vein samples were collected for analysis at four in situ sites from shore platform exposures in Waihou Bay (Figures 3 and 5). Vein samples ($n = 10$) were cut perpendicular to vein orientations, polished, and imaged under



Figure 5. Photos of typical occurrences of calcite veining and breccia in Tikiore Formation at Waihou Bay. Veins occur within zones of brecciated sandstone within and adjacent to normal faults. (a) Calcite veins and breccia in a normal fault trace marked with a red-dashed line. (b) Calcite veins orthogonal to bedding without evidence of a fault trace.

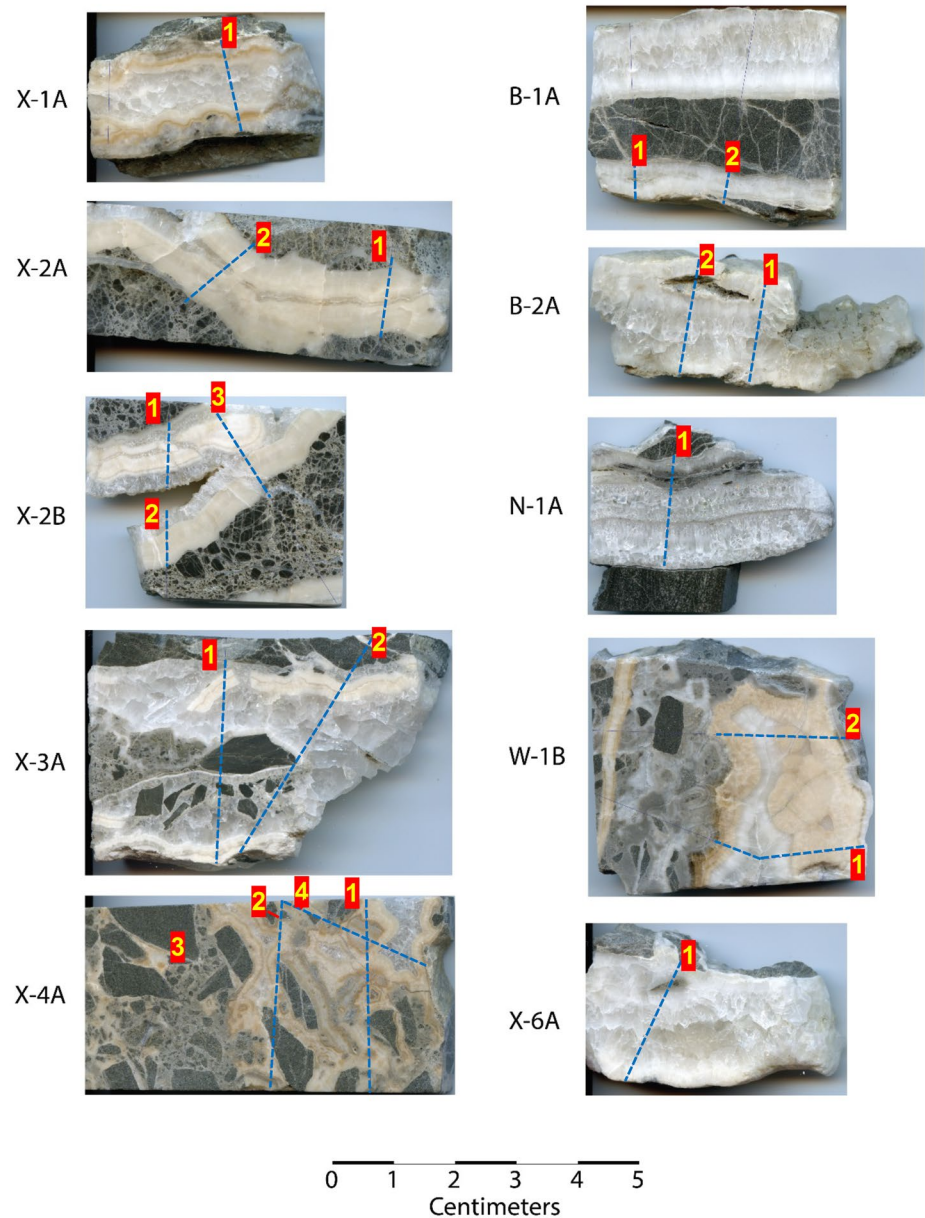


Figure 6. Photos of polished slabs evaluated in this study. These samples record evidence of hydraulic fracturing, focused fluid flow and calcite mineralization, with disruption and secondary infilling in and around earlier vein material. Blue-dashed lines denote ICP-MS transects referenced in the text. Red-highlighted number indicates the starting point of an ICP-MS transect. Samples exhibit deformation and veining events in three phases: (i) brecciation of the sandstone host rock and pervasive calcite cementation, (ii) infilling of fractures and breccia zones with a milky white to orange (plain light) laminar calcite, and (iii) disruption of milky and orange calcite and infilling of blocky white-clear calcite in the vein centers, leaving some vugs.

reflected light, cathodoluminescence light (CL), and ultraviolet (UV) light (Figures 6 and 7, and S1 in Supporting Information S1). Cathodoluminescence (CL) imaging was carried out using a CITL Mk5-1 cathodoluminescence stage attached to an optical microscope. The CL microscope was operated with an acceleration voltage of ~15 kV and a gun current of 200–240 μ A.

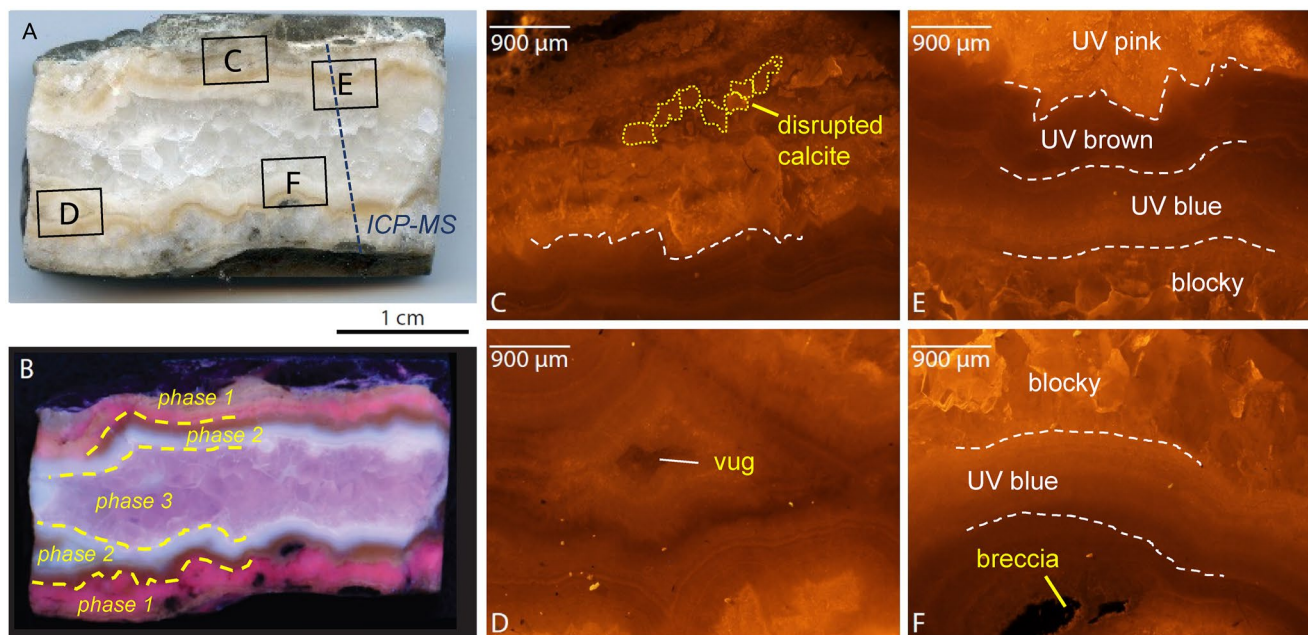


Figure 7. Polished slab of vein X1 in reflected light (a), ultraviolet (UV) light (b), and Cathodoluminescence (CL) light (c–f), highlighting carbonate textures. The blue line in panel A depicts the LA-ICPMS transect. Panel (b). UV light reveals four distinct zones. The rim zone, in contact with wall rock, is pink. This is followed by a thin band of brown laminated microcrystalline calcite, followed by a zone of very pale blue microcrystalline banded calcite. The vein center is infilled with a blocky white-clear calcite that is pale purple under UV. CL images (c–f) highlight crystal morphology within zones. Laminations within the blue and orange microcrystalline calcite are visible in all four CL images. For reference, the color boundaries on the UV image are drawn with a dashed white line between the pink and brown zones (c, e), brown and blue (e), and blue to blocky (e, f). Images of other samples in reflected light, UV light, and CL are provided in Figure S1 in Supporting Information S1.

3.2. Elemental Analysis and U-Pb Dating

The elemental geochemistry of vein samples was determined by Laser Ablation Induction Coupled Plasma Mass Spectrometry (LA-ICP-MS) at the University of Waikato. Analyses were carried out using an Agilent 8900 Triple Quadrupole ICP-MS, coupled with a Laurin Technic S155 SE ablation cell and a RESOLUTION 193 nm ArF excimer laser. Transects were measured across veins at a rate of 50 $\mu\text{m/s}$. All operating conditions are provided in Table S1 in Supporting Information S1. Elemental results were processed using *ioGAS*TM software and are reported in the analytical results section. Raw data are provided in the data repository.

Rare earth element patterns are used here to understand fluid source, fluid-rock interaction, and the oxidation state of fluids. Rare earth elements have been normalized to post Archean Australian Shale (PAAS) abundances (Taylor & McLennan, 1985). Anomalies were computed by comparing the shale-normalized value of a given element to the PAAS values of immediate neighbor elements on the REY spider diagram (Figure 8). For example, the shale normalized Eu anomaly is computed in the following:

$$\text{Eu}/\text{Eu}_{\text{SN}}^* = 2[\text{Eu}]_{\text{SN}}/[\text{Sm}]_{\text{SN}} + [\text{Gd}]_{\text{SN}}$$

U-Pb measurements of calcite veins were carried out by LA-ICP-MS as spot analyses. Within a given paragenetic zone, 20–60 spots were taken on transects along particular veins at 80–100 μm intervals. Spot analyses were taken at 30-s intervals with a pulse repetition rate of 10 Hz, a spot diameter of 100 μm , and a fluence of 7 J cm^{-2} . Data processing was carried out using the *Iolite*[®] software package (Paton et al., 2010). The SRM NIST 612 standard was used as a primary reference material. The calcite standard WC-1 with a reported age of 254.4 ± 6.4 Ma (Roberts et al., 2017) was used for U-Pb normalization.

3.3. Stable Isotope Analysis

Carbon and oxygen stable isotope measurements in calcite were carried out using a continuous flow laser spectroscopy approach modified from an analytical setup described by Barker et al. (2011) and Beinlich et al. (2017)

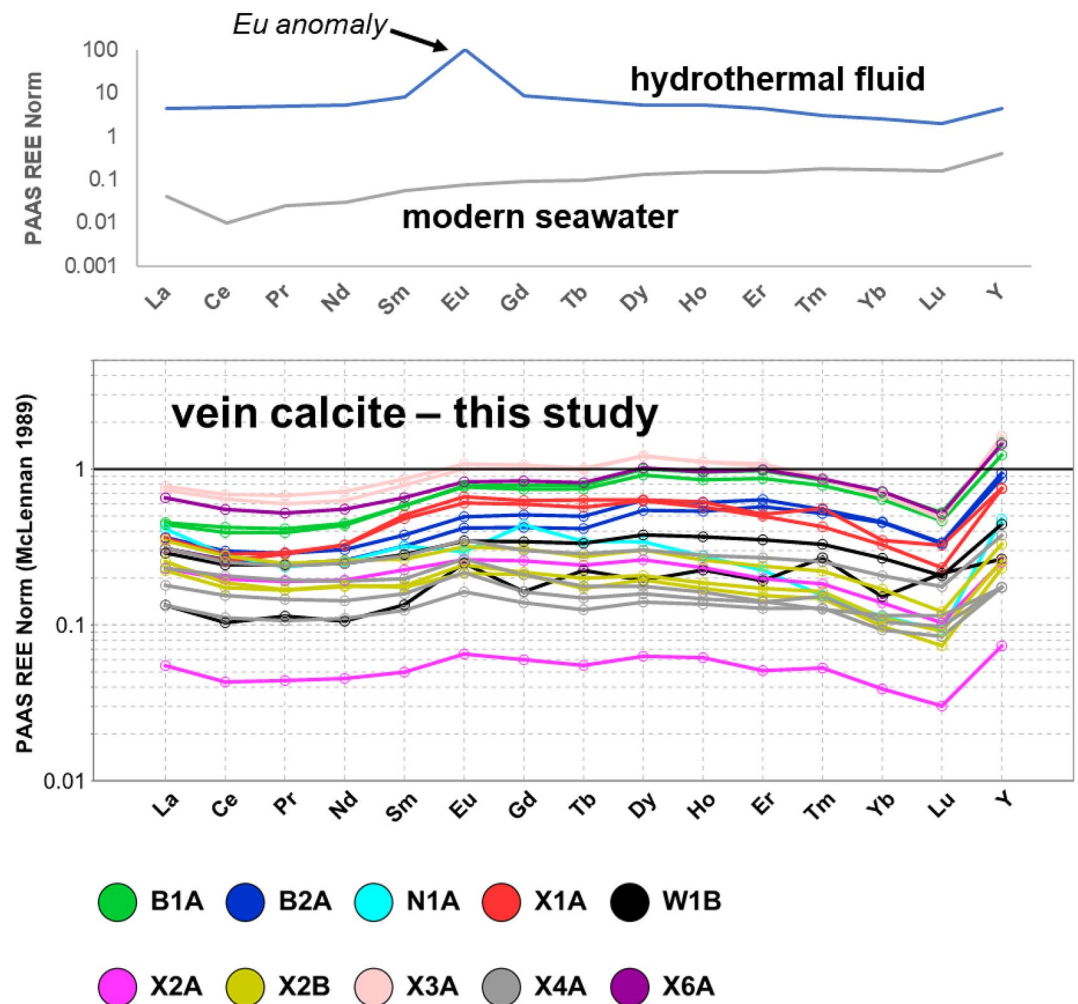


Figure 8. Representative spider diagram of rare earth elements plus Y (REY) abundances, normalized to post-Archaeon Australian Shale (PAAS) (Taylor & McLennan, 1985), derived from La-ICPMS spot analyses along the laser transects across 10 vein calcite samples (Figure 5). All values presented are mean values. The absence of a positive Eu anomaly suggests that there was no hydrothermal fluid source for the vein calcite. A positive Y excursion is a characteristic of a seawater-derived fluid source.

at the University of Waikato. Samples were digested in 102% orthophosphoric acid at 72°C in exetainer vials for a minimum of 2 hr prior to measurement. Sample CO₂ liberated from vein calcite was flushed from vials using a dual needle continuous flow system and passed through an ethanol-dry ice slush trap to remove water. Instrument operation parameters, reference materials, and raw analytical data are provided in Table S2 in Supporting Information S1 and the data repository. The typical precision of measurement for δ¹³C (±0.3‰ VPDB) and δ¹⁸O (±0.2‰ VPDB) was computed from the standard deviations of carbonate reference materials (RMs), which were run in duplicate.

3.4. Apatite Fission Track Analysis and Vitrinite Reflectance Analysis

Apatite fission track analysis (AFT) was applied to three samples (see Figure 3 for sample locations). The methods used for mineral separation and AFT dating of sample 1601-5 were the same as those described in Kamp (1999). The analyses and modeling were undertaken in the University of Waikato fission track laboratory. The age data for two of the samples (9601-69a and 9601-70a) have previously been reported together with apatite chlorine compositions (Kamp, 1999). Track lengths were remeasured. New AFT data are presented for one sample (1601-5), which together with the others help constrain the thermal history of the particular part of the Tikihore

Formation containing the calcite veins. Inverse modeling methods using HeFTy software v. 1.9.1 (Ketcham, 2005) were undertaken for all three sample AFT data sets. Stratigraphic constraints as described in Section 5.5 have been incorporated in the inverse models. The chlorine content of apatites in samples 9601-69a and -70 has been established by microprobe analysis as reported in Kamp (1999). For sample 9601-69a, the average wt.% Cl is 0.380 (range: 0.002–1.337) and for 9601-70a, it is 0.088 (range: 0.000–0.437). The AFT data have been modeled using a Durango Apatite Cl value of 0.4%. The graphical output for the thermal history modeling of the AFT data for sample (1601-5) is shown in Figure 9.

Vitrinite Reflectance (VIRF; vitrinite inertinite reflectance and fluorescence) was undertaken on plant-sourced macerals in each of four Tikiore Formation sandstone samples by Newman Energy Research Ltd under contract to University of Waikato. In the VIRF methodology, paired reflectance and fluorescence measurements were obtained on both vitrinite and inertinite (Newman, 1997). This method allows indigenous vitrinite of orthohydrous (“normal”) composition, which provides reliable reflectance data, to be distinguished from lower reflectance perhydrous vitrinite, which may have been altered during burial or oxidized (weathered) in the outcrop

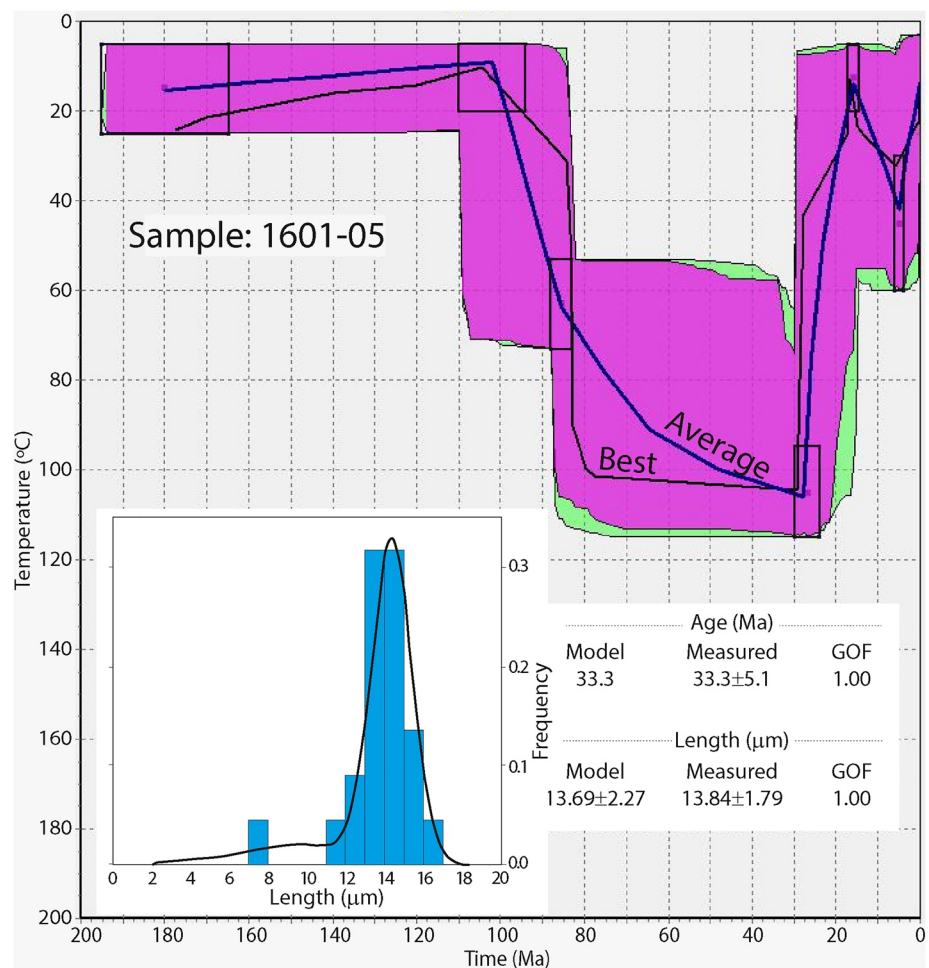


Figure 9. Apatite fission track thermal history model for sample 1601-5 from the Late Cretaceous Tikiore Formation (N.Z. Ngaterian Stage, 99.5–95.2 Ma) is produced with HeFTy software (Ketcham, 2005). This model and those of 9601-69a and 9601-70a (Figure S3 in Supporting Information S1) start with considerable provenance age, and sedimentation prior to 95 Ma. Maximum burial heating is constrained between 30 and 24 Ma, but the temperature is unconstrained. Exhumation of the sample host rock to the surface is constrained by the 16–15 Ma stratigraphic age of Clifdenian (15.9–15.1 Ma) neretic marine sediments west of outcrops of Tikiore Formation (Mazengarb & Speden, 2000). The late Miocene burial heating is broadly constrained to lie between 7.5 and 4 Ma, the age of inner shelf Mangaheia Group sediments overlying Tikiore Formation (Figure 3). The goodness of fit (GOF) is optimal at 1.0 for both age and length and the average and best model paths of 100,000 monte trax simulations are very similar. The purple zone represents good model results and the green margin represents acceptable model paths.

setting. Coals are the reference standards for VIRF measurements in terrigenous sediment samples (Newman et al., 2000). Rock samples for VIRF were crushed to <1 mm and mounted in polyester as 25-mm-diameter disks and then polished using a LECO (AP-60/VP150) polisher with the final polish attained with colloidal silica on a silk-covered bronze lap.

4. Description of Tikiore Formation Carbonate Veins

Carbonate veins occur in the lowermost part of the Tikiore Formation at Waihou Bay within normal fault zones, which displace highly indurated sandstone beds of Ngaterian and Arowhanan age (99.5–93.7 Ma) (Figure 3). Four examples of carbonate veins within normal faults (Figure 5) occur along a limited part of the rocky shore platform outlined in Figure 3.

The fault-hosted veins are exposed over distances of 2–3 m with up to 100 m of separation between occurrences. Veins are typically 0.5–2 cm in diameter. Larger brecciated zones, containing anastomosing carbonate veins, occur over a thicknesses of up to 30 cm. The veins in their field setting typically exhibit macroscopically zoned growth, including white to orange microcrystalline carbonate. In many cases, veins also contain a white to clear blocky textured carbonate in the vein centers, which does not always completely infill them.

4.1. Textural Observations and Phases of Vein Growth

Vein textures are described within three paragenetic phases of fracturing, dilation, and mineralization within the Tikiore Formation. Textural variations occur within these Phases 1–3, which are defined as subphases in Table 1. These subphases reflect the multistage history of deformation, fluid migration, and mineralization recorded by the Tikiore Formation. Table S3 in Table S1 provides more petrographic and textural details from both plane and UV light observations. However, for the purposes of placing the deformation and geochemical information recorded by the Tikiore veins into a regional tectonic context, we primarily refer to Phases 1–3. The ICP-MS transects and stable isotope data (i.e., $\delta^{13}\text{C}$ and $\delta^{18}\text{O}$) presented in the following sections encompass the opaque white and orange calcite material in Phase 2 and the blocky coarse calcite in Phase 3. Geochemical interpretations of these data are not made at the subphase level.

All vein phases are bright orange under CL (Figures 7 and S1 in Supporting Information S1), which is indicative of Mn^{2+} activation in calcite (e.g., Götze, 2012). When exposed to shortwave UV light, the vein infilling calcite exhibits a range of colors (Figures 7 and S1 in Supporting Information S1). XRD scans show that calcite is the only carbonate species present in all of the samples analyzed (Figure S2 in Supporting Information S1).

Phase 1 describes initial brecciation of the sandstone host rock and early cementation, typically composed of numerous thin anastomosing veinlets, giving the sandstone within, and immediately adjacent to normal fault zones, a distinctive pale gray color (Figures 5 and 6). The angular clasts produced during this initial phase of fracturing can also be internally calcite cemented although this is not always the case. The Phase 1 breccia and vein material is displaced by secondary brecciation, accompanied by episodic dilation and vein infilling with milky white and orange calcite (Phase 2). **Phase 2** calcite is frequently microcrystalline and finely laminated. This vein phase is pink, brown, and blue under UV light. Typically, Phase 2 calcite is present on both sides of veins as observed in cross section, and the outermost part in contact with the wall rock is commonly pink under UV

Table 1
Textures Present in Calcite Veins

	Phase	Subphase	Texture	X1	X2	X3	X4	X6	B1	B2	N1	W1
Vein chemistry assessed	1	1	Initial brecciation									
		2	White milky calcite									
	2	3	Brecciation									
		4	White milky calcite									
		5	Orange milky calcite									
		6	White milky calcite									
	3	7	Blocky white-clear calcite									
		8	Late veinlets									

Table 2
Select Major and Trace Elemental Abundances in Calcite Veins

Transect	Mg	Mn	Fe	Sr	Ba	Na	K	ΣREE
ALL	2,587	580	79	576	18	114	66	29
–	1,565	373	27	407	10	63	37	7
+	3,852	917	161	702	30	224	125	85
B1A-1	1,151	448	150	599	13	109	56	72
–	863	394	65	478	8	52	24	16
+	1,733	612	310	733	20	304	133	128
B1A-2	1,610	499	189	498	15	160	77	68
–	1,251	446	95	383	10	73	35	18
+	2,077	563	267	600	19	298	147	123
B2A-1	2,396	422	77	543	16	81	74	29
–	1,519	385	23	469	10	44	40	5
+	4,749	513	223	606	26	167	157	74
B2A-2	2,092	529	113	477	14	81	50	32
–	1,529	413	37	397	10	39	29	11
+	2,703	633	218	596	18	169	121	77
N1A-1	558	3,306	167	368	3	41	24	26
–	437	2,917	130	173	1	23	14	5
+	994	4,052	309	584	6	71	72	89
W1B-1	2,691	211	82	655	18	140	64	5
–	2,197	141	55	511	13	92	45	2
+	3,038	350	113	813	23	209	87	18
W1B-2	2,791	258	91	581	19	100	77	6
–	2,523	149	65	468	17	83	63	2
+	3,109	404	138	685	21	121	107	53
X1A-1	3,355	1,944	52	626	31	71	43	49
–	2,379	707	21	457	19	41	24	13
+	4,688	3,251	115	796	65	111	66	86
X1A-2	3,104	2,203	120	540	27	91	86	40
–	2,192	1500	51	453	18	67	57	7
+	4,024	4641	180	730	38	177	137	92
X2A-1	4,369	267	14	359	11	55	40	3
–	3,674	242	10	330	5	34	24	1
+	5,511	321	21	390	18	79	51	16
X2A-2	3,713	308	23	349	10	39	50	29
–	3,024	272	10	323	6	28	34	17
+	4,381	400	74	378	18	59	95	45
X2B-1	1,356	463	54	342	8	283	102	27
–	1,165	345	40	303	5	198	69	13
+	1,901	682	94	419	12	504	164	45
X2B-2	2,411	372	40	397	9	68	19	22
–	902	304	15	322	7	47	7	7
+	3,055	569	107	513	13	103	47	91
X2B-3	1,862	456	52	340	8	166	83	21

light (Figures 7 and S1 in Supporting Information S1). **Phase 3** encompasses vein mineralization of blocky white-clear calcite. This blocky calcite disrupts earlier milky white microcrystalline calcite and infills most vein centers although infilling is incomplete in some cases. The coarseness of these drusy calcite crystals and their incomplete infilling of vein cavities suggests that Phase 3 vein material represents the final significant period of fluid transmission through vein conduits. Minor and very thin late veinlets crosscut intact vein and breccia zones in some cases. In the following sections, we present the geochemistry of the primary vein infilling Phase 2 and 3 materials.

5. Results

5.1. Mineral Chemistry of Calcite Veins

Select major and trace elemental abundances as obtained from LA-ICP-MS analyses are reported in Table 2. ICP-MS transects across veins through the main infilling calcite of Phases 2 and 3 indicate that elemental concentrations vary from vein rim to center and in many cases are symmetrically zoned. A representative set of elemental transect data are presented for sample X1A in Figure 10, which shows that concentrations of Mg, Sr, and Ba increase in the orange band within the opaque microcrystalline calcite of Phase 2. Concentrations of Mn are elevated in the outer opaque white subphase of Phase 2, which is in contact with wall rock (>8,000 ppm), but strongly depleted in the subsequent orange and milky white microcrystalline subphases (<2,000 ppm), and in the blocky calcite of Phase 3 (~2,000–3,000 ppm) in the vein interior. Rare earth element abundance is lowest in the orange microcrystalline subphase in the center of Phase 2 and in the center of the blocky calcite of Phase 3 at the vein interior.

Spider diagram plots of calcite veins exhibit consistent patterns of relative enrichment or depletion for all samples (Figure 8). Median transect values of computed rare earth anomalies were near 1 for $[\text{Eu}/\text{Eu}^*]_{\text{PAAS}}$ (0.75–1.27), $[\text{Ce}/\text{Ce}^*]_{\text{PAAS}}$ (0.77–0.95), $[\text{Gd}/\text{Gd}^*]_{\text{PAAS}}$ (0.62–1.42), and $[\text{Er}/\text{Er}^*]_{\text{PAAS}}$ (0.85–1.11). REE concentrations do not vary significantly across the measured calcite veins (i.e., Phases 2–3). Here, values are computed for $[\text{Ce}/\text{Ce}^*]_{\text{PAAS}}$, $[\text{Gd}/\text{Gd}^*]_{\text{PAAS}}$, $[\text{Er}/\text{Er}^*]_{\text{PAAS}}$, and $[\text{Eu}/\text{Eu}^*]_{\text{PAAS}}$. Eu typically occurs in a 3+ oxidation state, but in reducing environments may attain 2+ valence. Strong positive Eu anomalies are indicative of mixing with hydrothermal fluids (e.g., German et al., 1993; Meyer et al., 2012; Tostevin et al., 2016). Small positive Eu anomalies of up to 1.5 are typical in fluids derived from seawater. The median Eu anomaly across all Tikiore Formation calcite transect measurements is 1.23, while the 25–75 percentile range is 1.02–1.23. The computed Eu anomaly exceeded 1.5 in less than 5% of transect measurements. Positive outliers for single measurements along transects either reflect local sample heterogeneity or counting statistics, given the relatively short integration time for spots along transects. The median Y/Ho value for all calcite vein transects is 39, while individual transects exhibited median values between 29 and 55 (Table 3). Y/Ho ratios are extremely consistent across paragenetic Phases 2 and 3. Modern seawater exhibits a strongly positive Y/Ho signature for calcite, typically greater than 36 (De Baar et al., 1985; Tostevin et al., 2016). Hence, both the Eu anomaly and Y/Ho ratio (Table 3; Figure S4 in Supporting Information S1) are consistent with a seawater-derived brine composition from which the calcite veins precipitated.

Table 2
Continued

Transect	Mg	Mn	Fe	Sr	Ba	Na	K	ΣREE
–	1,418	373	26	309	7	116	63	7
+	2,818	679	90	400	12	247	137	55
X3A-1	1,482	809	155	554	14	199	60	116
–	1,036	630	99	415	9	58	23	62
+	1,955	941	242	677	18	637	180	179
X3A-2	2,032	774	144	599	15	171	48	94
–	1,555	537	74	442	9	60	25	48
+	2,746	1,010	226	767	20	432	102	184
X4A-1	4,765	860	18	734	43	115	66	7
–	3,959	727	8	663	36	69	39	3
+	5,954	974	35	834	61	220	112	21
X4A-2	4,986	853	27	664	39	181	137	9
–	4,366	732	17	621	34	127	73	5
+	5,522	1,017	52	713	49	229	213	24
X4A-3	4,124	923	47	681	35	156	117	34
–	3,798	785	27	619	28	114	60	23
+	4,512	1,035	141	737	42	225	160	60
X4A-4	3,244	1,072	33	655	39	124	72	35
–	2,436	879	23	581	31	78	44	12
+	3,817	1,429	77	797	55	217	132	66
X6A-1	1,600	475	146	502	10	82	53	73
–	1,231	414	54	376	6	44	28	33
+	2,124	642	245	593	17	201	109	152

Note. Concentrations in parts per million (ppm). Values are median results for each transect. Ranges reflect 25 percentile (–) to 75 percentile (+). Elements in a given transect are normalised to the calcium concentration, assuming a Ca value of 40.3 weight percent.

5.2. Stable Isotope Composition of Calcite Veins

Oxygen and carbon stable isotope results are documented in Table 4 and are plotted in Figure 11. Raw data are available from the data repository. Oxygen isotope values ($\delta^{18}\text{O}$) range from -6.1 to $+8.4\text{‰}$ and are -0.2‰ VPDB on average. Carbon isotope values ($\delta^{13}\text{C}$) exhibit considerably greater variability across veins with values ranging between -28.0 and $+27.5\text{‰}$ and are -11.8‰ VPDB on average.

5.3. U-Pb Age of Calcite Veins

The U-Pb age of the Tikhore Formation calcite veins was calculated, following the method described in Parrish et al. (2018). In this approach, common ^{208}Pb is calculated by subtracting radiogenic ^{208}Pb from $^{208}\text{Pb}_{\text{total}}$. The amount of $^{208}\text{Pb}_{\text{radiogenic}}$ is calculated from the measured ^{232}Th , assuming closed-system behavior for ^{232}Th - $^{208}\text{Pb}_{\text{radiogenic}}$ decay. Subsequently, the $^{208}\text{Pb}_{\text{common}}/^{206}\text{Pb}$ is plotted against $^{238}\text{U}/^{206}\text{Pb}$. In this method, the x -intercept is the common Pb-corrected $^{238}\text{U}/^{206}\text{Pb}$ ratio. Multiple spot ages are plotted in an array of data for linear regression and intercept calculation using Isoplot (Ludwig, 2013). Parrish et al. (2018) demonstrated that this method results in smaller uncertainties and less regression scatter than in ^{207}Pb -corrected methods (e.g., Tera & Wasserburg, 1972). Lead ratio compositions at 0 and 85 Ma (Stacey & Kramers, 1975) have been applied to calculate the common Pb for each spot analysis. Common Pb ratios vary insignificantly within the 0–85 Ma period. We used common Pb ratios of 2.07 ± 0.02 for $^{208}\text{Pb}/^{206}\text{Pb}$ and 0.838 ± 0.02 for $^{207}\text{Pb}/^{206}\text{Pb}$ to anchor single spot analyses and to make the comparison between anchored and unanchored regression ages.

For quality control, $^{206}\text{Pb}_{\text{common}}$ was calculated from $^{208}\text{Pb}_{\text{common}}$ using the common Pb ratio described above. The value of $^{206}\text{Pb}_{\text{common}}$ was subsequently subtracted from $^{206}\text{Pb}_{\text{total}}$ to calculate $^{206}\text{Pb}_{\text{radiogenic}}$. If the value of $^{206}\text{Pb}_{\text{radiogenic}}$ was less than or equal to zero, a spot analysis was deemed unreliable and discarded. Analyses with $^{238}\text{U}/^{206}\text{Pb}$ uncertainty ellipses larger than 40% were also discarded. These cut-off criteria resulted in rejection of a large number of spot analyses. To derive a meaningful result, an aggregate age was calculated from all sample spot analyses for which the uncertainty ellipses were smaller than 40%. This approach assumes that vein

mineralization was a transient phenomenon. Some 48 spot analyses across three samples were used to calculate a weighted mean. A table with the measured and calculated values and calculated single spot ages for these 48 spots is provided in the data repository. The weighted mean age of the single spot analyses is 28.5 ± 4.9 Ma. Three of the spot analyses fell outside the error range of the weighted mean and these analyses were therefore regarded as outliers.

Forty-five spot analyses were used to calculate the regression age using the 86T-W plot. Figure 12 illustrates the single spot age results on the Parrish et al. (2018) 86T-W plot. This results in a common Pb anchored regression age of 28.5 ± 4.9 Ma (MSWD = 0.62; probability = 0.98), whereas the unanchored regression age is 21.9 ± 7.5 Ma (MSWD = 0.49; probability = 0.998). We have adopted the Pb-anchored regression age for interpretation, given its smaller error and larger MSWD values. Also, the unanchored regression age at face value is younger than the biostratigraphic age inferred for emplacement of the ECA (Mazengarb & Speden, 2000; Rait, 1992). The ages measured on the WC-1 standard are 258.8 ± 2.7 (MSWD = 0.94) using the 86T-W regression age and 251.7 ± 4.1 (MSWD = 1.08) using the conventional T-W regression age. Both are within error of the 254.4 ± 6.4 Ma age as reported by Roberts et al. (2017).

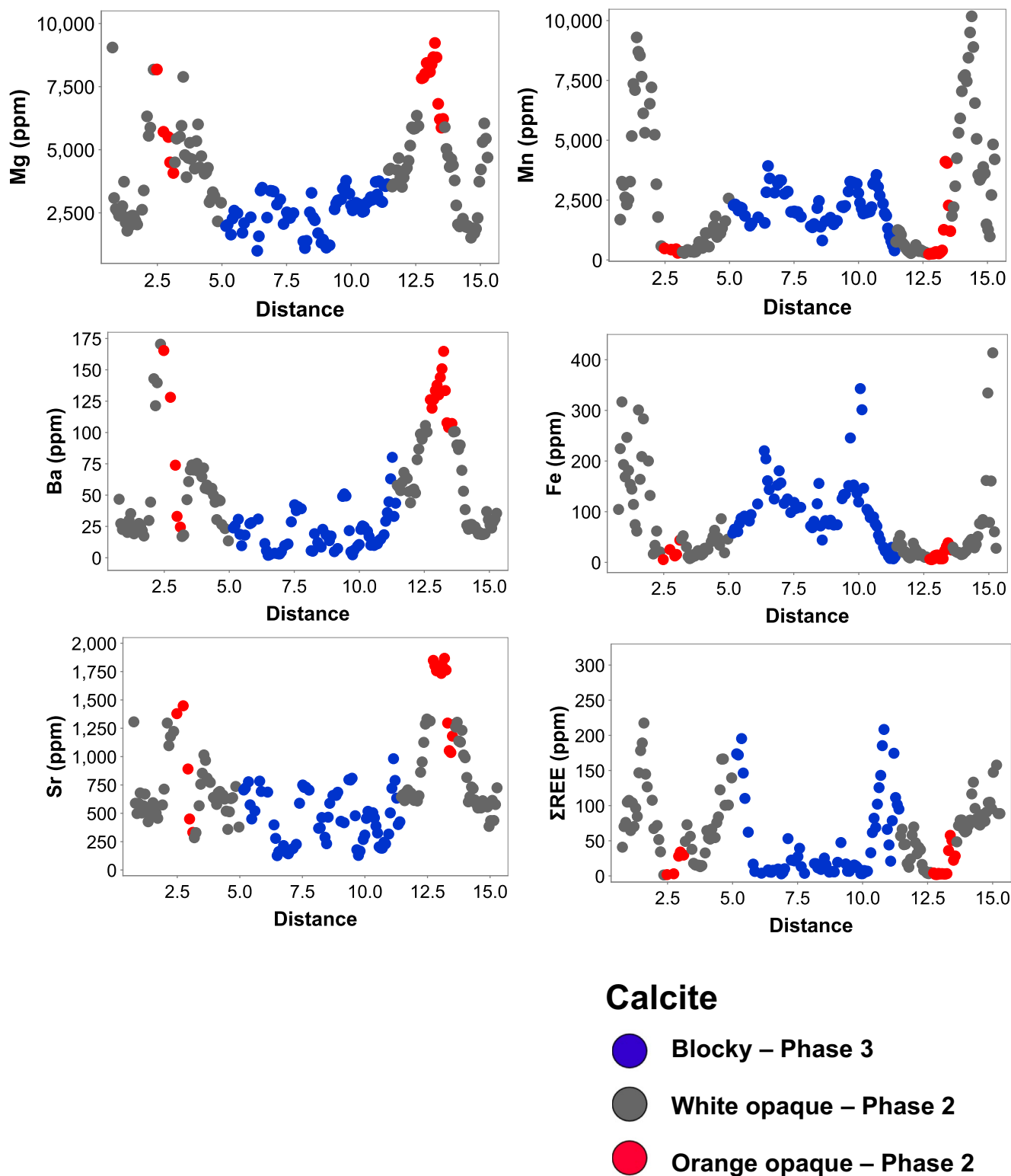


Figure 10. Abundance of major (Mg, Ba, Mn, Sr, and Fe) and trace elements (as sum of REE) for spot analyses by La-ICPMS along a line scan (Figure 6) of sample X1A (X1A-1). For each element, the spot data points are colored to distinguish the white and orange color zones (plain light) in Phase 2 calcite and the Phase 3 blocky calcite.

Table 3
Select REE Results

Transect	Y/Ho	Eu*	Ce*	Gd*	Er*
ALL	39.26	1.11	0.89	1.01	1.05
–	31.64	1.02	0.82	0.90	0.95
+	48.68	1.23	0.96	1.11	1.12
B1A-1	42.40	1.13	0.93	1.00	1.09
–	36.48	1.06	0.86	0.91	1.04
+	49.79	1.20	0.99	1.09	1.14
B1A-2	42.53	1.12	0.94	1.00	1.08
–	35.17	1.05	0.89	0.94	1.03
+	50.81	1.19	1.00	1.08	1.13
B2A-1	46.04	1.09	0.89	1.02	1.08
–	36.76	1.01	0.80	0.96	1.02
+	61.10	1.19	0.98	1.10	1.15
B2A-2	45.91	1.10	0.88	1.04	1.11
–	35.96	1.02	0.80	0.93	1.05
+	59.14	1.19	0.94	1.12	1.18
N1A-1	53.57	0.75	0.82	1.42	1.07
–	40.68	0.69	0.68	1.25	0.99
+	65.28	0.85	0.94	1.60	1.14
W1B-1	37.52	1.25	0.77	0.62	0.85
–	23.98	0.99	0.48	0.20	0.36
+	51.53	4.79	0.89	1.00	1.09
W1B-2	37.95	1.10	0.89	1.00	1.02
–	31.07	1.01	0.83	0.90	0.96
+	46.47	1.22	0.93	1.07	1.09
X1A-1	34.17	1.08	0.85	1.01	0.96
–	28.58	1.00	0.78	0.84	0.80
+	44.54	1.27	0.90	1.10	1.03
X1A-2	37.30	1.07	0.87	1.04	1.00
–	32.48	1.01	0.81	0.98	0.98
+	54.13	1.12	0.91	1.11	1.05
X2A-1	39.30	1.06	0.83	1.04	0.98
–	29.37	0.93	0.77	0.87	0.82
+	48.89	1.33	0.88	1.22	1.06
X2A-2	30.96	1.07	0.91	1.03	0.97
–	25.59	1.01	0.88	0.96	0.91
+	38.41	1.15	0.94	1.11	1.02
X2B-1	37.19	1.10	0.88	1.06	1.04
–	30.07	0.99	0.80	0.97	0.96
+	48.79	1.22	0.92	1.20	1.15
X2B-2	36.79	1.10	0.91	1.04	1.03
–	30.15	1.02	0.86	0.96	0.96
+	43.90	1.21	0.99	1.11	1.10
X2B-3	37.88	1.09	0.87	1.08	1.03

5.4. Maximum Burial Temperature of Tikiore Formation and Timing of Cooling

To help constrain the host rock's maximum burial temperature(s) and the timing of the start of cooling, we obtained apatite fission track (AFT) and vitrinite reflectance data for a suite of sandstone samples from Tikiore Formation. Both methods are regarded as standard approaches for assessing the thermal history of sedimentary rocks. The AFT results are given in Table 5 and the VIRF results are given in Table 6.

As the ECA has a disrupted stratigraphy, constraints on the depth of burial of Tikiore Formation for use in the HeFTy thermal history modeling of AFT data can only be estimated from the Late Cretaceous–late Oligocene stratigraphy in deep drill hole Rere-1 (Figure 2), drilled into autochthonous strata immediately south of the ECA (Field et al., 1997). This drill hole intersected 1,920 m of 100–86 Ma section, overlapping in age with the Tikiore Formation exposed at Waihou Bay, and 1,680 m of 85–23 Ma section that accumulated post subduction as an overlying passive margin succession (Tinui and Maungatu groups; Figure 4). We use the two Rere-1 stratigraphic packets and their ages to constrain the Late Cretaceous–Oligocene heating in our HeFTy models (Figure 9 and S3 in Supporting Information S1).

The timing of the start of cooling of the Tikiore Formation is constrained between 30 and 24 Ma. The older limit is older than any suggestions in the literature about the timing of the start of the modern plate boundary in New Zealand and ECA emplacement; the younger limit is close to the Oligocene–Miocene boundary, which was previously regarded as when the modern plate boundary formed (e.g., Carter & Norris, 1976; Cooper et al., 1987; Field et al., 1997; Kamp, 1986). The end of the early Miocene cooling phase is constrained to be c. 14 Ma based on the unconformable accumulation of neretic mid-Miocene (Lillburnian Stage, 15.10–13.05 Ma) strata over Cretaceous accretionary wedge rocks (Pahau Terrane) located immediately east of Waihou Bay (Mazengarb & Speden, 2000). The amount of middle and late Miocene burial heating (Figure 9) is not prescribed, but the timing of its peak is constrained to be within 7.5–4 Ma, based on the timing of the start of regional uplift and erosion of Raukumara Peninsula (Mazengarb & Speden, 2000), which led to the current exposure of Tikiore Formation at Waihou Bay. Sample 1601-5 is from a location immediately east of the vein calcite occurrences (Figure 3). The measured AFT age for this sample is 33.0 ± 5.0 Ma, much younger than the stratigraphic age (99.5–95.2 Ma; Ngaterian Stage) of the sample host sandstone, but only about 5 m.y. older than its likely cooling age prior to incorporation into the ECA. This age, together with a measured mean track length around 13.8 microns, and the occurrence of some short tracks (7–8 microns), suggests qualitatively that the fission tracks were not fully annealed at the point of maximum burial; that is, the maximum burial temperature did not reach the total resetting temperature of about 110°C for fission tracks in apatite of Durango composition. The HeFTy thermal history model for sample 1601-5 indicates a maximum burial temperature of about 105°C and a start of cooling at around 28 Ma. We adopt the average path in the HeFTy model to read the maximum temperature and the timing of the start of cooling. The middle to late Miocene burial heating peaked at about 45°C at 5 Ma, prior to cooling of the host rock to the surface. The goodness-of-fit (GOF) values for this HeFTy model are 1.0 for both age and length, and the “Average” and “Best” paths of 100,000

Table 3
Continued

Transect	Y/Ho	Eu*	Ce*	Gd*	Er*
–	29.42	0.98	0.82	0.98	0.94
+	48.42	1.22	0.95	1.21	1.13
X3A-1	40.00	1.10	0.93	1.03	1.06
–	34.21	1.05	0.85	0.98	1.02
+	45.42	1.15	1.01	1.09	1.10
X3A-2	42.06	1.09	0.94	1.04	1.10
–	35.25	1.05	0.88	0.98	1.06
+	46.88	1.15	1.00	1.11	1.13
X4A-1	41.93	1.14	0.87	1.00	1.05
–	32.83	0.98	0.81	0.81	0.80
+	52.48	1.38	0.93	1.14	1.17
X4A-2	36.66	1.27	0.88	0.92	1.01
–	29.73	1.10	0.81	0.65	0.78
+	45.91	1.64	0.95	1.06	1.16
X4A-3	28.76	1.22	0.95	0.96	1.03
–	22.48	1.11	0.90	0.81	0.88
+	35.00	1.37	1.00	1.09	1.09
X4A-4	37.04	1.16	0.91	0.97	1.02
–	31.16	1.07	0.85	0.88	0.90
+	43.49	1.30	0.95	1.05	1.10
X6A-1	40.74	1.10	0.91	1.03	1.09
–	34.81	1.05	0.87	0.97	1.05
+	48.03	1.15	0.96	1.09	1.12

Note. Rare Earth Element anomalies are calculated relative to shale normalised abundances (PAAS). Values are median results for each transect. Ranges reflect 25 percentile (–) to 75 percentile (+).

Monte Carlo simulations are similar, giving a high level of confidence in the peak burial temperature reached and the timing of the 28 Ma start of cooling (Figure 9).

Sample 9601-69a has statistically similar AFT parameters of age and track length with those for sample 1601-5 and they were not reset at the time of peak burial heating. The HeFTy model result indicates a peak burial temperature of about 104°C compared with 105°C for 1601-5 (Figure S3 in Supporting Information S1). The constraint box for 9601-69a was set at 32–25 Ma with the modeled average path cooling starting at c. 30 Ma. The GOF values are 0.92 for age and 0.70 for track length.

Sample 9601-70a was collected from a site on the western side of Orete Point more distant from the calcite vein locations than the other two AFT samples within the Arowhanan part of Tikiore Formation (Figure 3). The measured fission track age is 17.9 ± 5.1 Ma with a mean track length of 12.21 ± 1.57 microns. The measured age indicates that the AFT parameters were reset leading up to the peak of burial heating, suggesting that the formation temperature at that point exceeded 110°C. As the measured age is younger than the likely late Oligocene age of peak heating, the AFT data cannot resolve the amount and timing of peak heating. The HeFTy model (Figure S3 in Supporting Information S1) does however show middle and late Miocene burial heating to 82°C at about 4 Ma, which shortened the track lengths to 12.21 ± 1.57 microns. The GOF for the 9601-70a model is 1.00 for both age and track length.

We now consider vitrinite reflectance data (Table 6) for each of four samples. Sample UW-1 is from a thick-bedded turbidite at the same outcrop as AFT sample 1601-5 (Figure 3). Parts of sample UW-1 are heavily iron stained with framboidal pyrite altered to iron oxide, indicative of recent weathering. The VIRF chart for UW-1 features both oxidized and unoxidized organic assemblages. Normal vitrinite in sample UW-1 of 1.42% Ro (normal) clusters toward the high reflectance end of the normal vitrinite compositional range and is consequently considered to have a high bias as some oxidized vitrinite grains are probably included in this Ro (normal) value. Thermal history modeling using HeFTy and the burial history shown for 1601-5, but varying the input maximum temperature at 28 Ma, gives a peak of about 140°C well in excess of that estimated from modeling of the AFT data for 1601-5 (c. 105°C).

Sample UW-4 is a moderately carbonaceous siltstone that exhibits considerable iron staining on weathered surfaces, but internal surfaces are unaffected and most pyrite is unaltered. This sample was collected from the same site as sample 9601-70a (Figure 3). The Ro (normal) value for this sample is 1.32%. The HeFTy modeling of this vitrinite data using the same burial history for 9601-70a, but varying the input temperature at 27 Ma, gives a maximum burial temperature of 125°C.

Sample UW-2 was taken from a turbidite sandstone bed on the shore platform close to Orete Point (Figure 3) and lies in the Teratan (90.5–86.5 Ma) part of Tikiore Formation; that is, at a stratigraphic level above the vein calcite occurrences. The measured vitrinite reflectance Ro (normal) is 0.72%, and together with inertinite data, forms a well-defined curve. The thermal history modeling using a similar burial history as for AFT sample 9601-69a, but varying the input maximum burial temperature at 30 Ma, results in a paleotemperature of about 110°C for UW-2. This is a slightly higher paleotemperature value than expected, given its higher stratigraphic position in Tikiore Formation compared with samples 9601-69a and 1601-5 of 105°C and 104°C, respectively.

Sample UW-3 is from the highest stratigraphic level (Piripauan, 86.5–83.6 Ma) in Tikiore Formation exposed at Waihou Bay. This sandstone sample is from a turbidite with obvious plant material aligned with parallel laminations. It has unaltered pyrite and the Ro (normal) VR value is 0.72% based on an unbiased normal vitrinite assem-

Table 4
Calcite Vein Isotope Results

Sample	$\delta^{13}\text{C}$ (‰ VPDB)	$\delta^{18}\text{O}$ (‰ VPDB)	Inferred temperature range (°C)		
			T at 0‰ VSMOW	T at 3.5‰ VSMOW	T at 6‰ VSMOW
N1B					
<i>N1B.1</i>	7	8.4	−23	−10	0
<i>N1B.2</i>	−21.5	−0.1	12	29	42
X1B					
<i>X1B.1</i>	−21.9	1.8	3	19	31
<i>X1B.2</i>	−14.2	−0.2	12	29	42
<i>X1B.3</i>	−6.6	1.4	5	21	34
<i>X1B.4</i>	14.3	−1.2	17	35	48
X2C					
<i>X2C.1</i>	−19.9	−0.9	16	33	47
<i>X2C.2</i>	−20.9	−1.8	20	38	52
<i>X2C.3</i>	−21.2	−3	26	45	59
<i>X2C.4</i>	−10.4	−2.8	25	43	58
X2D					
<i>X2D.1</i>	−2.8	−0.1	12	29	42
<i>X2D.2</i>	−19.1	−0.3	13	30	43
<i>X2D.3</i>	−18.1	−1.4	18	36	49
<i>X2D.3rep</i>	−18.2	0.3	10	27	40
<i>X2D.4</i>	−11.2	0.1	11	28	41
<i>X2D.5</i>	−6.1	−0.9	16	33	47
<i>X2D.6</i>	−6.2	3	−2	13	25
X3B					
<i>X3B.1</i>	−3	1.7	4	20	32
<i>X3B.2</i>	−19.7	−6.1	43	64	80
<i>X3B.3</i>	−12.9	−3.1	27	45	60
<i>X3B.3rep</i>	−13.9	−2.4	23	41	56
<i>X3B.4</i>	−12.7	0.6	9	25	38
<i>X3B.5</i>	−18.2	−1.8	20	38	52
<i>X3B.6</i>	−21.1	−0.4	13	30	44
X4B					
<i>X4B.1</i>	0.2	−3.5	29	48	62
<i>X4B.2</i>	−13.5	−2.3	23	41	55
<i>X4B.3</i>	−14.6	−2.3	23	41	55
<i>X4B.4</i>	−19.3	−1.8	20	38	52
<i>X4B.5</i>	−11.6	−0.7	15	32	45
W1A					
<i>W1A.1</i>	−17.7	−2.3	23	41	55
<i>W1A.2</i>	22.2	4.9	−9	5	16
<i>W1A.3</i>	−26	1.2	6	22	35
<i>W1A.3rep</i>	−27.7	2.3	1	17	29
<i>W1A.4</i>	−28	−0.6	14	31	45

blage. With the same measured Ro value as for sample UW-2, the maximum temperature estimate would be about 110°C, also higher by 5°C than would be expected from the AFT modeling of samples 1601-5 and 9601-69a.

6. Discussion

6.1. Isotopic Constraints Upon Vein Mineralization Environment

Carbon isotope values reflect source material and the redox conditions in the fluid that precipitated vein calcite. A number of terrestrial carbon sources overlap with the $\delta^{13}\text{C}$ results for veins measured here (Figure 11). Overall, the results reflect two distinct processes common in sedimentary environments. More negative carbon isotope values (less than -10‰ VPDB) are consistent with sourcing from microbially mediated oxidized buried organic matter (approximately -30 to -10‰ VPDB) or, potentially, thermogenic methane (-50 to -20‰ VPDB) (e.g., Budai et al., 2002; Drake et al., 2015). The positive $\delta^{13}\text{C}$ values measured, in excess of $+20\text{‰}$ VPDB, in several vein samples are significantly more enriched than marine and geothermal-hydrothermal CO_2 (Figure 11). The most extremely positive $\delta^{13}\text{C}$ values in the Tikhore Formation veins reflect mineralization from a highly enriched dissolved inorganic carbon (DIC) pool, resulting from bacterial methanogenesis (Budai et al., 2002; Drake et al., 2015). The enriched DIC was either sourced locally in vug spaces in vein interiors or flowed from elsewhere in the reservoir. Under semi or fully closed-system conditions within vug spaces in vein interiors, microbial processing of isotopically lighter carbon may have progressively enriched the $\delta^{13}\text{C}$ of the residual DIC.

The oxygen isotope composition of calcite reflects the isotope composition of source fluids as well as the fluid temperature at the time of vein mineralization. We apply three fluid $\delta^{18}\text{O}$ composition scenarios to the data set reported here (Figure 11). In the first scenario, fluids involved in hydraulic fracturing and vein mineralization in the Tikhore Formation were likely trapped marine pore waters that migrated through the upper part of the evolving wedge and did not undergo any isotopic enrichment. Second, present-day saline spring fluids within the Hikurangi margin that exhibit $\delta^{18}\text{O}$ values of $+3.5\text{‰}$ VSMOW on average (Barnes et al., 2019; Gigenbach et al., 1995; Reyes et al., 2010) are plotted. We also consider the possibility that the veins formed from a more enriched sedimentary brine of $+6\text{‰}$ VSMOW, analogous to deep continental fluids (Kharaka & Hanor, 2003). Some degree of enrichment above 0‰ VSMOW would not be atypical. We apply these three fluid compositional ranges (i.e., ~ 0 to $+3.5\text{‰}$ or 0 to $+6\text{‰}$ VSMOW) to establish the likely fluid temperature range at the time of vein mineralization shown in red in Figure 11. Based on this analysis, we derive the following upper bounds for fluid temperature: 29°C if we assume the fluid is an unevolved seawater at 0‰ VSMOW, 48°C assuming mineralization from average Hikurangi saline springs with a $\delta^{18}\text{O}$ value of $+3.5\text{‰}$ VSMOW, or 62°C assuming an evolved continental sedimentary brine at $+6\text{‰}$ VSMOW. From this, we infer that the fluid temperature during mineralization of the calcite veins in Tikhore Formation most likely lay between 29°C and 48°C , but may have been as high as 62°C if the fluid were isotopically enriched.

6.2. Degree of Cooling of Tikhore Formation Before Vein Formation

One purpose of estimating the burial temperatures for selected horizons in Tikhore Formation was to better characterize the degree of cooling that

Table 4
Continued

Sample	$\delta^{13}\text{C}$ (‰ VPDB)	$\delta^{18}\text{O}$ (‰ VPDB)	Inferred temperature range (°C)		
			T at 0‰ VSMOW	T at 3.5‰ VSMOW	T at 6‰ VSMOW
W1A.5	-23.5	1.1	7	23	35
B1B					
B1B.1	-6.8	3.1	-2	13	25
B1B.2	-13.2	4.4	-7	7	18
B1B.3	-6.2	-0.3	13	30	43
B1B.4	27.5	5.5	-12	2	13
B2B					
B2B.1	-9.8	-0.3	13	30	43
B2B.2	-16.6	-5.2	38	58	74

Note. Average 1σ of $\delta^{13}\text{C}$ and $\delta^{18}\text{O}$ are 0.3 and 0.2‰, respectively. Vein temperatures determined using fractionation factor in Kim & O'Neil, 1997.

must have preceded the formation of the carbonate veins described here and the peak burial temperature of Tikiore Formation. AFT samples 1601-5 and 9601-69a stratigraphically and geographically bracket the exposures where the calcite veins were described and sampled and we use the modeled peak burial temperature of the more conservative slightly lower value ($104 \pm 10^\circ\text{C}$; cf., $105 \pm 10^\circ\text{C}$) to calculate the maximum burial temperature of Tikiore Formation and the difference between it and the vein calcite fluid temperature range at the time of calcite precipitation. The VRIF results provide an upper bound on the maximum burial temperature but they are consistently higher and more variable than those estimated from modeling of the apatite fission track data. Therefore, we adopt the fission track temperatures ($104 \pm 10^\circ\text{C}$) as more realistic. For the vein mineralization temperature, rather than taking the fluid temperature values (29°C , 48°C , and 62°C) marked on Figure 11b, we have computed the mean and standard deviation temperature values at 0‰ VSMOW, +3.5‰ VSMOW, and +6‰ VSMOW from each of the sample calcite $\delta^{18}\text{O}$ results (‰ VPDB); that is, using all of the data (see data repository). The computed mean and SD temperature values are $13 \pm 13^\circ\text{C}$ at 0‰ VSMOW, $30 \pm 14^\circ\text{C}$ at +3.5‰ VSMOW, and $43 \pm 16^\circ\text{C}$ at +6‰ VSMOW. These temperature ranges are lower than those marked in Figure 11b because they use all of the isotope data as opposed to the upper temperature bound of the red box in Figure 11b. The important

observation is that the computed mean temperature values and their ranges are low compared with the maximum burial temperature estimate ($104 \pm 10^\circ\text{C}$) for Tikiore Formation, indicating that most of the exhumation of Tikiore Formation must have preceded vein mineralization.

The matrix offset temperature between the conservative peak burial temperature ($104 \pm 10^\circ\text{C}$), taking account of the associated error range, and the vein mineralization temperature and its range for the +3.5‰ VSMOW estimate ($30 \pm 14^\circ\text{C}$; adopted for this calculation as it is based on the average $\delta^{18}\text{O}$ value composition of modern saline spring fluids in the Raukumara region) is 114°C – 16°C and 94°C – $44^\circ\text{C} = 98^\circ\text{C}$ – 50°C . This offset temperature range for a geothermal gradient of 25°C indicates 2.0–3.9 km of erosion of rock section from above the structural level of Tikiore Formation before the vein mineralization occurred. This compares with a total amount of 3.8–4.6 km of exhumation of Tikiore Formation based on its peak burial temperature of $104 \pm 10^\circ\text{C}$. Hence, only about 0.1–1.8 km of exhumation of Tikiore Formation postdated the calcite vein mineralization. As the U-Pb age of the vein calcite overlaps with the modeled AFT age of exhumation (30–27 Ma), the early unloading of rock section and the subsequent hydraulic fracturing and vein mineralization occurred in quick succession within the age range we can resolve for these events.

6.3. Triggering Mechanisms for Calcite Vein Growth

Field and petrographic observations, and geochemical analyses, indicate that the formation of calcite veins in Tikiore Formation involved hydraulic fracturing within normal fault zones, fluid migration, and calcite mineralization. The symmetric UV fluorescence patterns and elemental zonation across veins imply isotropic mineral growth that initiated at the outer margins of fractures and grew inward with blocky calcite partially to fully infilling vein centers during Phase 3. These patterns are consistent with a crack-seal formation mechanism (e.g., Oliver & Bons, 2001; Ramsay, 1980), where fracturing and dilation are followed by rapid infilling and mineral growth.

Some degree of fluid pumping through the fractures may also explain the development of the vein infilling textures in Tikiore Formation. Multiple brecciation and fluid events are inferred from Tikiore Formation vein samples that show deformation of early phase infills (Table 1; Figure 6). The so-called valve model (e.g., Lee & Morse, 1999; Sibson, 1990) holds that the greatest vein growth rates occur during rapid fluid flow events along fractured channels. Given the relatively large diameter (>1 cm) of many veins in Tikiore Formation, it is likely that fluid flow and mineral infilling occurred during multiple short-lived events. Episodic pulses enable rapid migration of fluids at, or near, calcite saturation (Lee & Morse, 1999).

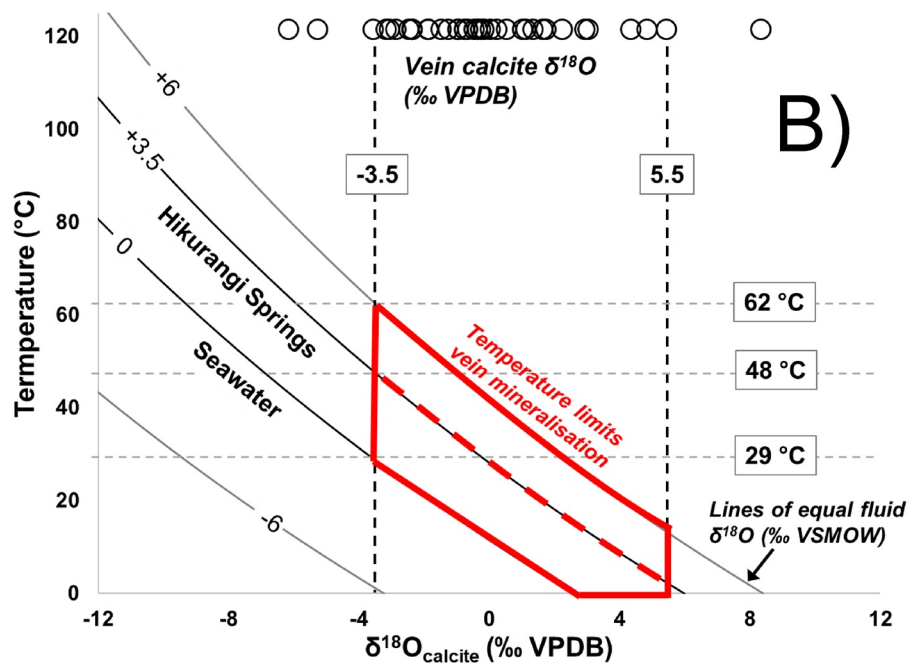
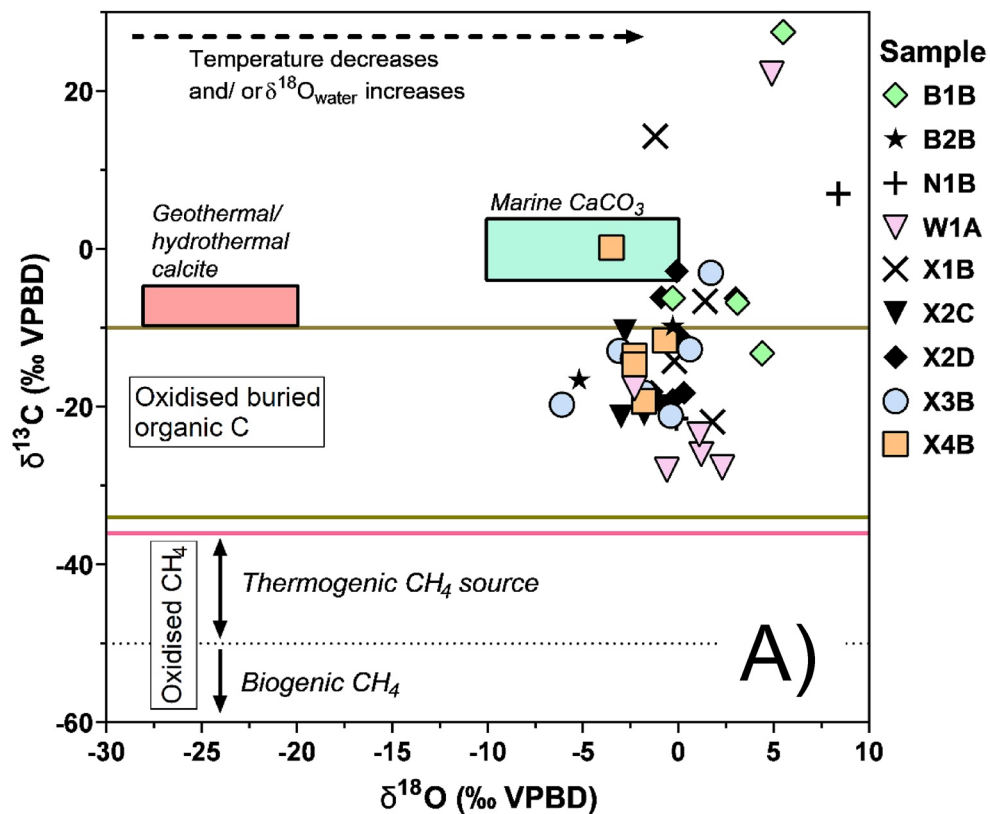


Figure 11.

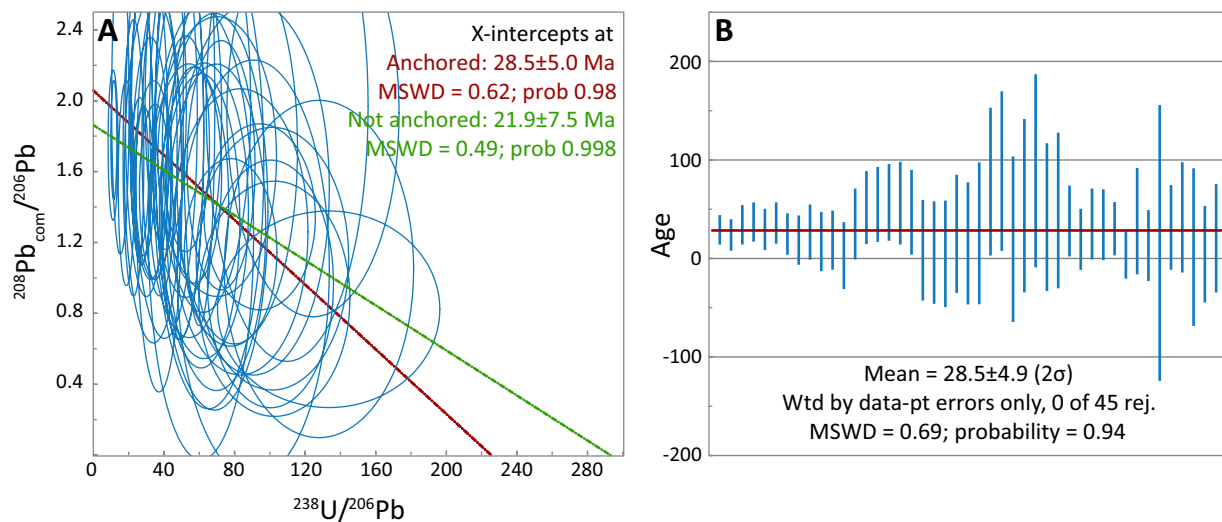


Figure 12. U-Pb age relationships determined for calcite veins from Tikihore Formation. Uncertainty ellipses and error bars are 2σ of the mean. (a) 86T-W plot determined using the method described in Parrish et al. (2018). The red line is the regression line with common Pb anchored, while the green line is the unanchored regression line. (b) Weighted mean plot of single spot ages corrected using the ^{208}Pb method described in Parrish et al. (2018).

6.4. Exhumation and Associated Uplift Within the Hikurangi Margin

The location of the convergent plate boundary at the Late Cretaceous termination of subduction along the New Zealand sector of East Gondwana has been mapped by seismic reflection methods at depth along parts of the Hikurangi margin (Barnes et al., 2010). It lies inboard of the Hikurangi Trough (trench), reflecting subsequent Neogene outbuilding of the modern subduction margin. Tikihore Formation accumulated in an accretionary slope basin located immediately inboard of the Late Cretaceous Gondwana plate edge (Mazengarb & Harris, 1994). We interpret the vein calcite U-Pb age and the AFT modeled age range of 30–27 as dating the start of exhumation of Tikihore Formation, related to uplift of the edge of the plate at that time. Exhumation of Tikihore Formation was probably achieved by slumping of the weakly to moderately consolidated overlying sedimentary succession (Tinui and Ruatoria groups; Figure 4) off the Tikihore Formation as originally envisaged by Stoneley (1968). Figure 13 is a schematic representation of this succession of events. The early slumping process markedly reduced the lithostatic load on the fluid reservoir (either in the Tikihore Formation or in the underlying accretionary wedge), which reduced the effective stress such that the already existing fluid pressure in the reservoir was able to fracture (hydraulic fracturing) the Tikihore Formation. Our observation that calcite veins with zones of brecciation lie within normal fault zones suggests that hydraulic fracturing exploited normal faults probably associated with slumping of cover rocks from above the Tikihore Formation.

Prior work has established that the ECA was emplaced from the NE (offshore) to the SW (Rait, 1992; Stoneley, 1968) into a forearc basin, inboard, and higher up on the Australia Plate than the elevation of the lower slope position where its sediment content accumulated. Based on its mapped extent (Mazengarb & Speden, 2000), the ECA has a length of 150 km, a width of 60 km, and a thickness of about 2 km, amounting to an approximate $18,000 \text{ km}^3$ volume. These factors require considerable uplift near the mid-Oligocene edge of the Australia Plate. We speculate that this uplift was driven by the start of subduction of the oceanic Pacific Plate beneath the outer edge of the continental Australia Plate (Figure 13).

Figure 11. Carbon and oxygen isotope results for Tikihore Formation calcite vein analyses. Panel (a) $\delta^{18}\text{O}$ – $\delta^{13}\text{C}$ results plotted alongside the values of major terrestrial reservoirs. The brown lines bound the typical $\delta^{13}\text{C}$ values of oxidized terrestrial organic matter. The red horizontal line denotes the upper limit of $\delta^{13}\text{C}$ in methane. The horizontal dashed line within the methane $\delta^{13}\text{C}$ domain defines the boundary between thermogenic and biogenic formation processes. The red box defines the range of values for high-temperature calcite in modern North Island geothermal systems (Simmons & Christenson, 1994). The green box defines the range of calcite and aragonite precipitating from ocean water. In general, a move to the right for $\delta^{18}\text{O}$ reflects decreasing mineralization temperature or increases in the oxygen isotope values of fluids. The carbon isotope value ranges are from Wagner et al. (2018). Panel (b) Illustration of Tikihore Formation vein calcite fluid-mineral oxygen isotope temperature relationships. Contours of equal fluid $\delta^{18}\text{O}$ contours are plotted. The red polygon denotes the range of fluid $\delta^{18}\text{O}$ (‰ VSMOW) and temperature conditions consistent with the oxygen isotope results for calcite (‰ VPDB) reported here. The fluid-calcite $\delta^{18}\text{O}$ fractionation factor in Kim and O’Neil (1997) was used to generate fluid-temperature outcomes.

Table 5
Apatite Fission Track Results

Sample number	Number of crystals	Spontaneous		Induced		P(χ^2) %	ρ_s/ρ_i		ρ_d	Nd	Age (Ma) $\pm 1\sigma$	Mean track length $\pm 1\sigma$ (μm)	Standard deviation (μm)	Number of lengths
		ρ_s	Ns	ρ_i	Ni		$\pm 1\sigma$							
1601-5	30	0.487	230	2.364	1117	98.18	-	0.929	2203	33.3 \pm 2.6	13.84 \pm 1.79	1.51	100	
9601-69a	20	0.458	448	1.699	1662	<0.1	0.230 \pm 0.023	0.873	4315	40.3 \pm 4.6	14.22 \pm 1.79	1.70	56	
9601-70a	15	0.227	56	1.904	469	63.2	-	0.873	4315	17.9 \pm 2.3	12.21 \pm 1.57	1.67	8	

Note. Track densities (ρ) are $\times 10^6$ tracks cm^{-2} . All analyses are by the External Detector Method using 0.5 for the $4\pi/2\pi$ geometry correction factor. Apatite ages calculated using dosimeter glass SRM 612 and zeta-612 = 343.5 \pm 4.5 ($\pm 1\sigma$). P(χ^2) is the probability of obtaining χ^2 value for ν degrees of freedom (where ν is the number of crystals -1) (Galbraith, 1981); pooled ρ_s/ρ_i ratio is used to calculate age and uncertainty where P(χ^2) >5%; mean ρ_s/ρ_i ratio is reported for samples where P(χ^2) <5% and for which Central ages (Galbraith & Green, 1990) are calculated.

Geodynamic models of subduction initiation involving oblique convergence predict the uplift of the overriding plate followed by its subsidence (Gurnis et al., 2004; Toth & Gurnis, 1998). Shuck et al. (2022) have recently demonstrated this sequence of events for initiation of the Puysegur subduction margin, which is the subduction zone at the southern end of the Alpine Fault (Figure 3). It has opposite polarity to the Hikurangi margin. We suggest that the Shuck et al. (2022) geological model for subduction initiation at the Puysegur margin also applies to the Hikurangi margin, in particular the uplift of the leading edge of the overriding plate as the first manifestation of subduction initiation and subsidence of the margin as the second manifestation. A difference however is that the Puysegur margin appears to have evolved out of a fault, whereas the Hikurangi margin involved subduction initiation at a continental margin that was formerly the outer edge of the upper plate of a Cretaceous subduction zone.

6.5. Supporting Evidence for Hikurangi Margin Subduction Initiation During the Mid-Oligocene?

Here we discuss other geological evidence in support of our 30–27 Ma age range of subduction initiation at the Hikurangi margin. Figure 14 is a map of Zealandia at 27 Ma with the Australia Plate fixed and 800 km of late Oligocene and Neogene displacement and deformation through New Zealand restored, consistent with reconstructions by Bradshaw (1989) and King (2000). The development of the Australia-Pacific plate boundary through New Zealand occurred during two phases. The first, from 43 to 30 Ma, involved a diverse plate boundary system from south to north through western New Zealand that linked spreading in the Emerald Basin and South Tasman Sea (Cande & Stock, 2004; Keller, 2005; Weissel et al., 1977) to a continental rift in western South Island (the Challenger Rift System; Kamp, 1986), to a foreland basin (Taranaki Foreland Basin; King & Thrasher, 1996), to a zone of structural inversion (Reinga Basin; Bache et al., 2012), and to a subduction zone immediately west of New Caledonia (Schellart et al., 2006; Van de Lagemaat et al., 2018). The change in tectonic character northward along this plate boundary zone is reflected in the central New Zealand location of finite rotation poles for 40–35 and 34–30 Ma (Figure 14). These poles lie within the uncertainty ellipses derived by Keller (2005) from small circles to transform faults offsetting the Macquarie Spreading Centre in the Emerald Basin.

The second tectonic phase started with the 30–28 Ma end of east-dipping subduction in the New Caledonia margin and the start of west-dipping subduction along the new Tonga-Kermadec subduction zone (Van de Lagemaat et al., 2018). The Tonga-Kermadec subduction zone rolled back to its present position northeast of Raukumara Peninsula during the early Miocene accompanied by back-arc spreading in the South Fiji Basin

Table 6
VRIF Results

Sample ID	Ro (normal) %	s.d.	Range %	Confidence	Criteria for confidence ratings
UW-1	1.42 ($n = 18$)	0.123	1.17–1.56	Good	Multiple vitrinite populations, inertinite support
UW-2	0.72 ($n = 11$)	0.112	0.58–0.90	Good+	Well defined VIRF curve including inertinite support
UW-3	0.72 ($n = 11$)	0.138	0.56–0.93	Good+	Well defined VIRF curve including inertinite support
UW-4a	1.32 ($n = 19$)	0.092	1.17–1.44	Good+	Well defined VIRF curve including inertinite support

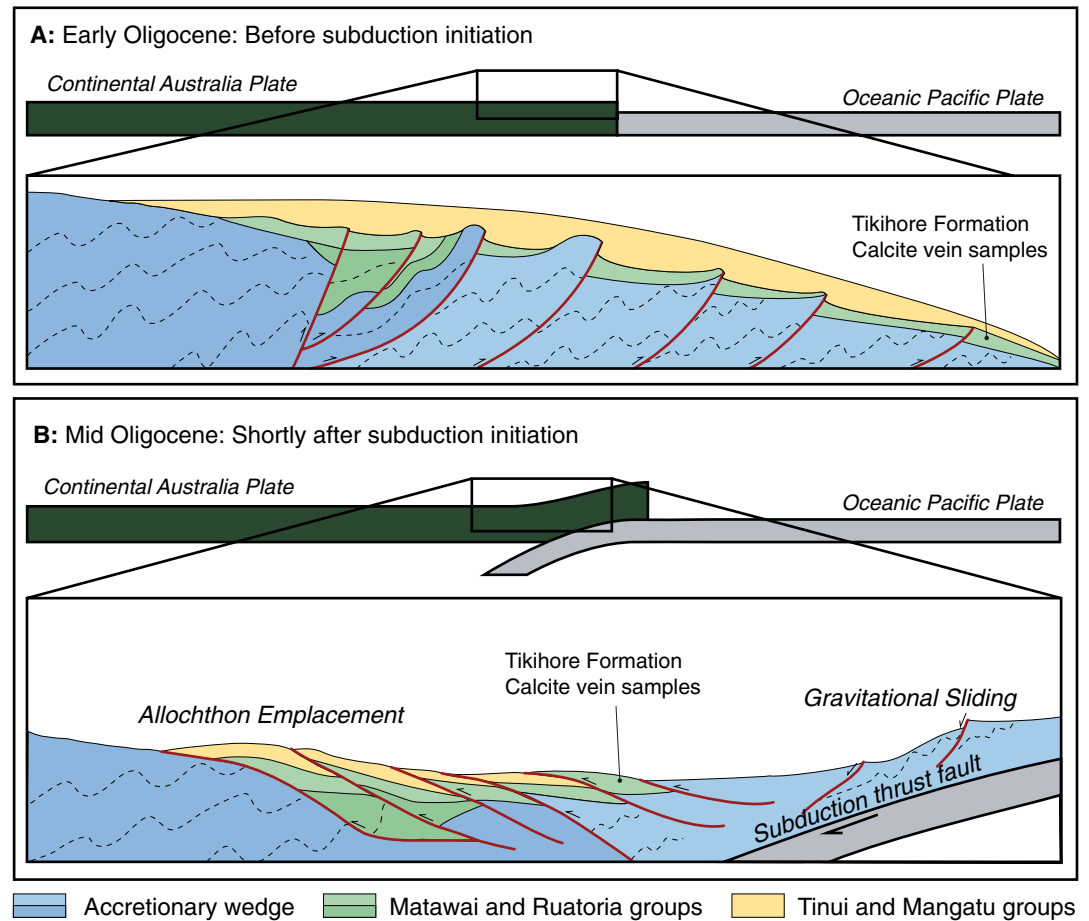


Figure 13. Schematic illustration showing in Panel A the continent-ocean juxtaposition during the early Oligocene before initiation of Pacific Plate subduction. The Torlesse Complex accretionary wedge including its basins (Matawai Group) formed during the Cretaceous involving Phoenix Plate subduction below East Gondwana. The Tinui and Mangatu groups accumulated during the latest Cretaceous and Paleogene as passive margin sediments. Panel B shows mid-Oligocene initiation of Pacific Plate subduction with uplift of the leading edge of Australia Plate, leading to gravitational sliding of the sedimentary section and part of the accretionary wedge (Mokoiwi Formation) off the structural high, forming the East Coast Allochthon on the Australia Plate.

(Herzer et al., 2011; Mortimer et al., 2007; Van de Lagemaat et al., 2018) and post 7 Ma spreading in the Lau-Havre Trough (Anderson et al., 2021) (Figure 1).

During 30–27 Ma, the Tonga-Kermadec subduction zone linked southward to the Hikurangi margin, which formed along the continent-ocean boundary of northeastern North Island (Figure 14). By 26 Ma, the Hikurangi margin had linked to the Alpine Fault, which cut obliquely across the more northerly trend of the former Challenger Rift System (Kamp, 1986). A set of finite rotation poles describing the 26 Ma onward relative motion between the Australia and Pacific plates along this second plate boundary zone are reported in Cande and Stock (2004). Furlong and Kamp (2009) derived stage poles at 1 m.y. intervals from these finite rotation poles. It is difficult to derive definitive stage poles for the interval 30–26 Ma because of the increasingly oblique deformation that occurred during the late stages of spreading along the Macquarie Spreading Center (Cande & Stock, 2004) and also because of post-spreading deformation that distorted the transform faults offsetting the spreading ridge along the modern plate boundary zone (Hayes et al., 2009; Keller, 2005). Nevertheless, Furlong and Kamp (2009, 2013) did report them for this interval, but we adopt here a parsimonious pole route for the interval of 30–26 Ma (Figure 14). After 26 Ma, the stage poles rapidly migrated to the southeast toward the Present-day Euler pole (Furlong & Kamp, 2009).

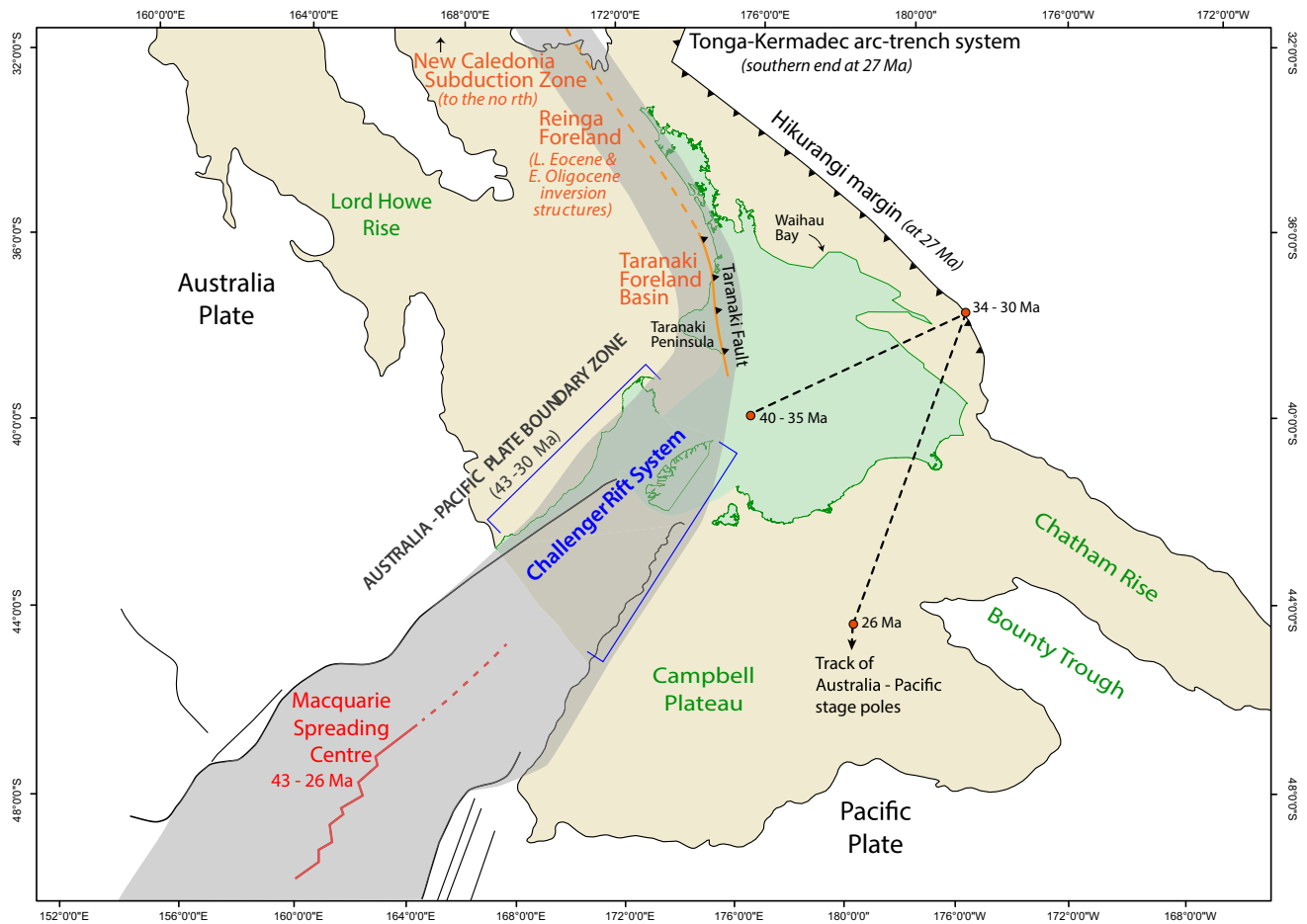


Figure 14. In this map, the Australia Plate is fixed relative to the Pacific Plate, and the continental crust of Zealandia, shown in light brown, is referenced to the current latitude and longitude as though it is all Australia Plate. The deformation taken up within the modern Australia-Pacific plate boundary zone has been restored with the conservation of area of the onland extent of New Zealand, shown in green, at 27 Ma. The map shows in a gray swath the western New Zealand extent and tectonic character of the initial (45–30 Ma) Australia-Pacific plate boundary zone through New Zealand. After 30 Ma, the Hikurangi margin formed part of a second plate boundary zone, which linked to the Alpine Fault and Puysegur Subduction Zone (neither shown here). See the text for discussion about the poles of rotation.

At 30 Ma, the finite rotation pole lay on or near what would become part of the Hikurangi margin. Our study area at Waihou Bay and the likely position of the sedimentary and volcanic succession that became the ECA lay to the north of that pole position (Figure 14). During 30–26 Ma, the direction of the pole track implies increasing rates of convergence at the Hikurangi margin. This margin also lengthened southward during this interval (Figure 14). It is reasonable therefore that sometime after 30 Ma and by 27 Ma, convergent relative plate motion would have been expressed as subduction initiation along the Hikurangi Margin.

Taranaki Basin (Figure 14), located immediately west of Taranaki Fault (King & Thrasher, 1996), carries a stratigraphic and structural record of both phases of plate boundary development through New Zealand. During 43–30 Ma, Taranaki Basin lay within the plate boundary zone and a foredeep developed along its eastern part beneath northern Taranaki Peninsula and the part of the basin farther north (King & Thrasher, 1996). This foredeep was loaded by basement beneath the Tongaporutu-Herangi High to its east, this structural high forming from upper crustal thickening within the Taranaki Fault Zone (Stagpoole & Nicol, 2008). After 30 Ma, Taranaki Fault was well oriented to accommodate displacement as a backthrust to the Hikurangi Margin (Figure 14).

Strogen et al. (2019) have recently reported the development of a new foredeep during c. 30–27 Ma, centered over the southern part of the peninsula and immediately south of it. They relate this new phase of subsidence to an unconformity developed within a piggy-back basin succession immediately east of the Herangi High (Kamp et al., 2014). We consider that the development of this second foredeep in Taranaki Basin, related to renewed

thrusting within the Taranaki Fault Zone, reflects strain transferred through the crust of North Island from shortening at the nascent Hikurangi subduction zone.

7. Conclusions

1. Syntectonic vein calcite within normal fault zones that offset turbidite beds in Tikiore Formation on the rocky shore platform at Waihou Bay, northern Raukumara Peninsula, precipitated during rapid fluid flow associated with hydraulic fracturing.
2. The trace metal content and rare earth element patterns established for the calcite veins are consistent with a seawater-derived brine composition with no evidence of hydrothermal conditions.
3. The positive $\delta^{13}\text{C}$ values of the calcite veins of up to +28‰ VDPB reflect contemporary methanogenesis and preferential processing of isotopically lighter carbon remaining in the vein reservoir following the early phases of vein precipitation, which depleted its original more negative $\delta^{13}\text{C}$ content.
4. Oxygen isotope ($\delta^{18}\text{O}$) values of the vein calcite range from -6.1 to $+8.4$ ‰ and are -0.2 ‰ VPDB on average. Reasoning that the $\delta^{18}\text{O}$ composition of the fluids at the time of calcite mineralization likely lay between ~ 0 and $+3.5$ ‰ VSMOW on average (based on the composition of modern sea water vs. saline spring fluids, respectively, in the Raukumara region) the upper bound of mineralization likely occurred at temperatures between 29°C and 48°C . Alternatively, using all of the sample calcite $\delta^{18}\text{O}$ ‰ VPDB results, the mean and SD calcite fluid temperature values at mineralization are calculated to have been $13 \pm 13^\circ\text{C}$ at 0‰ VSMOW and $30 \pm 14^\circ\text{C}$ at $+3.5$ ‰ VSMOW. Both methods of deriving mineralization temperature estimates are markedly less than the maximum burial temperatures experienced by the host rocks, which we estimate to be $104 \pm 10^\circ\text{C}$ from the inverse modeling of apatite fission track data, supported by the results of vitrinite reflectance data.
5. A calcite vein has been U-Pb dated by LA-ICP-MS, yielding an age of 28.5 ± 4.9 Ma (MSWD = 0.62; probability = 0.98), using a common Pb-anchored regression.
6. We attribute fracturing and fluid migration to rapid decompression of the fluid reservoir due to the removal by submarine slumping of several km of stratigraphic section above Tikiore Formation and associated normal faulting, the slump material then contributing to the East Coast Allochthon, ultimately emplaced in a more inboard part (forearc basin) of the Australia Plate.
7. We infer the start of subduction at the Hikurangi margin to lie in the range of 30–27 Ma, consistent with the 30–28 Ma age of formation of the Tonga-Kermadec arc-trench system immediately to the north and the 30–27 Ma timing of a new phase of shortening across the Taranaki Fault Zone and related foredeep development in eastern Taranaki Basin.

Acknowledgments

We wish to acknowledge with gratitude the *Maru-o-Hinemaka (Parariki)* hapu and particularly John Butler for facilitating the field component of our research and the provision of accommodation and hospitality at the Raukokore Education Center. We wish to gratefully acknowledge the following people for their technical assistance with data acquisition and analysis: Kirsty Vincent for XRD analyses, Ben Andrews for stable isotope analyses, Merijn van Logtestijn for U-Pb dating, Xu Ganqing for AFT analyses, and Newman Research Ltd for VIRF analyses. We thank Douwe van Hinsbergen for a helpful internal review of the manuscript prior to its submission. This project was funded by the New Zealand Government (MBIE Contract: CONT-42907-EMTR-UOW), including the funding of a 6-month fellowship to SvL at the University of Waikato. We thank three reviewers and the associate editor for their constructive reviews that helped us to improve this manuscript.

Data Availability Statement

All raw LA-ICP-MS and stable isotope data are available from the data repository associated with this manuscript (Van de Lagemaat et al., 2021; <http://doi.org/10.17632/tjhzpdkvmp.1>).

References

- Anderson, M. O., Norris-Julseth, C., Rubin, K. H., Haase, K., Hannington, M. D., Baxter, A. T., & Stewart, M. S. (2021). Geologic and structural evolution of the NE Lau Basin, Tonga: Morphotectonic analysis and classification of structures using shallow seismicity. *Frontiers in Earth Sciences*, 9, 665185. <https://doi.org/10.3389/feart.2021.665185>
- Bache, F., Sutherland, R., Stagpoole, V., Herzer, R., Collot, J., & Rouillard, P. (2012). Stratigraphy of the southern Norfolk Ridge and the Reinga Basin: A record of initiation of Tonga-Kermadec-Northland subduction in the southwest Pacific. *Earth and Planetary Science Letters*, 321–322, 41–53. <https://doi.org/10.1016/j.epsl.2011.12.041>
- Ballance, P. F. (1976). Evolution of the upper Cenozoic magmatic arc and plate boundary in northern New Zealand. *Earth and Planetary Science Letters*, 28(3), 356–370. [https://doi.org/10.1016/0012-821X\(76\)90197-7](https://doi.org/10.1016/0012-821X(76)90197-7)
- Ballance, P. F. (1993). *South Pacific sedimentary basins* (p. 143). Elsevier.
- Ballance, P. F., Hayward, B. W., & Brook, F. J. (1985). Subduction regression of volcanism in New Zealand. *Nature*, 313(6005), 820. <https://doi.org/10.1038/313820a0>
- Ballance, P. F., & Spörli, K. B. (1979). Northland allochthon. *Journal of the Royal Society of New Zealand*, 9(2), 259–275. <https://doi.org/10.1080/03036758.1979.10419416>

- Barker, S. L., Cox, S. F., Eggins, S. M., & Gagan, M. K. (2006). Microchemical evidence for episodic growth of antitaxial veins during fracture-controlled fluid flow. *Earth and Planetary Science Letters*, 250(1–2), 331–344. <https://doi.org/10.1016/j.epsl.2006.07.051>
- Barker, S. L., Dipple, G. M., Dong, F., & Baer, D. S. (2011). Use of laser spectroscopy to measure the $^{13}\text{C}/^{12}\text{C}$ and $^{18}\text{O}/^{16}\text{O}$ compositions of carbonate minerals. *Analytical Chemistry*, 83(6), 2220–2226. <https://doi.org/10.1021/ac103111y>
- Barnes, J. D., Cullen, J., Barker, S., Agostini, S., Penniston-Dorland, S., Lassiter, J. C., et al. (2019). The role of the upper plate in controlling fluid-mobile element (Cl, Li, B) cycling through subduction zones: Hikurangi forearc, New Zealand. *Geosphere*, 15(3), 642–658. <https://doi.org/10.1130/GES02057.1>
- Barnes, P. M., Lamarche, G., Bialas, J., Henrys, S., Pecher, I., Netzeband, G. L., et al. (2010). Tectonic and geological framework for gas hydrates and cold seeps on the Hikurangi subduction margin, New Zealand. *Marine Geology*, 272(1–4), 26–48. <https://doi.org/10.1016/j.margeo.2009.03.012>
- Beach, A. (1980). Numerical models of hydraulic fracturing and the interpretation of syntectonic veins. *Journal of Structural Geology*, 2(4), 425–438. [https://doi.org/10.1016/0191-8141\(80\)90004-8](https://doi.org/10.1016/0191-8141(80)90004-8)
- Beinlich, A., Barker, S. L., Dipple, G. M., Gupta, M., & Baer, D. S. (2017). Stable isotope ($\delta^{13}\text{C}$, $\delta^{18}\text{O}$) analysis of sulfide-bearing carbonate samples using laser absorption spectrometry. *Economic Geology*, 112(3), 693–700. <https://doi.org/10.2113/econgeo.112.3.693>
- Bradshaw, J. D. (1989). Cretaceous geotectonic patterns in the New Zealand region. *Tectonics*, 8(4), 803–820. <https://doi.org/10.1029/TC008i004p00803>
- Brothers, R. N., & Delaloye, M. (1982). Obducted ophiolites of North Island, New Zealand: Origin, age, emplacement and tectonic implications for tertiary and Quaternary volcanicity. *New Zealand Journal of Geology and Geophysics*, 25(3), 257–274. <https://doi.org/10.1080/00288306.1982.10421491>
- Brown, K. M., Bekins, B., Clennell, B., Dewhurst, D., & Westbrook, G. (1994). Heterogeneous hydrofracture development and accretionary fault dynamics. *Geology*, 22(3), 259–262. [https://doi.org/10.1130/0091-7613\(1994\)022<0259:HHDAAF>2.3.CO;2](https://doi.org/10.1130/0091-7613(1994)022<0259:HHDAAF>2.3.CO;2)
- Budai, J. M., Martini, A. M., Walter, L. M., & Ku, T. C. W. (2002). Fracture-fill calcite as a record of microbial methanogenesis and fluid migration: A case study from the Devonian Antrim Shale, Michigan basin. *Geofluids*, 2(3), 163–183. <https://doi.org/10.1046/j.1468-8123.2002.00036.x>
- Campbell, K. A., Farmer, J. D., & Des Marais, D. (2002). Ancient hydrocarbon seeps from the Mesozoic convergent margin of California: Carbonate geochemistry, fluids and palaeoenvironments. *Geofluids*, 2(2), 63–94. <https://doi.org/10.1046/j.1468-8123.2002.00022.x>
- Campbell, K. A., Francis, D. A., Collins, M., Gregory, M. R., Nelson, C. S., Greinert, J., & Aharon, P. (2008). Hydrocarbon seep-carbonates of a Miocene forearc (East Coast basin), North Island, New Zealand. *Sedimentary Geology*, 204(3–4), 83–105. <https://doi.org/10.1016/j.sedgeo.2008.01.002>
- Cande, S. C., & Stock, J. M. (2004). Pacific—Antarctic—Australia motion and the formation of the Macquarie Plate. *Geophysical Journal International*, 157(1), 399–414. <https://doi.org/10.1111/j.1365-246X.2004.02224.x>
- CANZ. (2008). *New Zealand region Bathymetry, 1:4 000 000* (2nd ed.). NIWA Chart, Miscellaneous Series No. 85.
- Carter, R. T., & Norris, R. J. (1976). Cainozoic history of southern New Zealand: An accord between geological observations and plate-tectonic predictions. *Earth and Planetary Science Letters*, 31(1), 85–94. [https://doi.org/10.1016/0012-821X\(76\)90099-6](https://doi.org/10.1016/0012-821X(76)90099-6)
- Cooper, A. F., Barreiro, B. A., Kimbrough, D. L., & Mattinson, J. M. (1987). Lamprophyre dike intrusion and the age of the Alpine fault, New Zealand. *Geology*, 15(10), 941–944. [https://doi.org/10.1130/0091-7613\(1987\)15<941:LDIATA>2.0.CO;2](https://doi.org/10.1130/0091-7613(1987)15<941:LDIATA>2.0.CO;2)
- Crampton, J. S. (1996). *Inoceramid bivalves from the Late Cretaceous of New Zealand* (Vol. 14, pp. 74–165). Institute of Geological and Nuclear Sciences Monograph.
- De Baar, H. J. W., Bacon, M. P., Brewer, P. G., & Bruland, K. W. (1985). Rare Earth elements in the Pacific and Atlantic Oceans. *Geochimica et Cosmochimica Acta*, 49(9), 1943–1959. [https://doi.org/10.1016/0016-7037\(85\)90089-4](https://doi.org/10.1016/0016-7037(85)90089-4)
- Drake, H., Åström, M. E., Heim, C., Broman, C., Åström, J., Whitehouse, M., et al. (2015). Extreme ^{13}C depletion of carbonates formed during oxidation of biogenic methane in fractured granite. *Nature Communications*, 6(1), 1–9. <https://doi.org/10.1038/ncomms8020>
- Edbrooke, S. W., Heron, D. W., Forsyth, P. J., & Jongens, R. (2015). *Geological map of New Zealand 1:1 000 000. GNS Science geological map 2. 2 sheets*. GNS Science.
- Farsang, S., Louvel, M., Zhao, C., Mezouar, M., Rosa, A. D., Widmer, R. N., et al. (2021). Deep carbon cycle constrained by carbonate solubility. *Nature Communications*, 12(1), 1–9. <https://doi.org/10.1038/s41467-021-24533-7>
- Field, B. D., Uruski, C. I., Beu, A. G., Browne, G. H., Crampton, J. S., Funnell, R., et al. (1997). *Cretaceous-Cenozoic geology and petroleum systems of the East Coast region, New Zealand*. In *Institute of Geological & Nuclear Sciences Monograph 19*. Institute of Geological & Nuclear Sciences, Lower Hutt.
- Francis, D. A. (1995). Oil and gas seeps of northern and central East Coast Basin. *Petroleum Exploration in New Zealand News*, 44, 21–27.
- Furlong, K. P., & Kamp, P. J. (2009). The lithospheric geodynamics of plate boundary transpression in New Zealand: Initiating and emplacing subduction along the Hikurangi margin, and the tectonic evolution of the Alpine Fault system. *Tectonophysics*, 474(3–4), 449–462. <https://doi.org/10.1016/j.tecto.2009.04.023>
- Furlong, K. P., & Kamp, P. J. (2013). Changes in plate boundary kinematics: Punctuated or smoothly varying—evidence from the Mid-Cenozoic transition from lithospheric extension to shortening in New Zealand. *Tectonophysics*, 608, 1328–1342. <https://doi.org/10.1016/j.tecto.2013.06.008>
- Galbraith, R. F. (1981). On statistical models for fission track counts. *Journal of the International Association for Mathematical Geology*, 13(6), 471–478. <https://doi.org/10.1007/BF01034498>
- Galbraith, R. F., & Green, P. F. (1990). Estimating the component ages in a finite mixture. *International Journal of Radiation Applications and Instrumentation. Part D. Nuclear Tracks and Radiation Measurements*, 17(3), 197–206. [https://doi.org/10.1016/1359-0189\(90\)90035-V](https://doi.org/10.1016/1359-0189(90)90035-V)
- German, C. R., Higgs, N. C., Thomson, J., Mills, R., Elderfield, H., Blusztajn, J., et al. (1993). A geochemical study of metalliferous sediment from the TAG hydrothermal Mound, 26°08'N, mid-Atlantic Ridge. *Journal of Geophysical Research*, 98(B6), 9683–9692. <https://doi.org/10.1029/92JB01705>
- Giggenbach, W. F., Stewart, M. K., Lyon, G. L., Sano, Y., & Goguel, R. L. (1995). Isotopic and chemical composition of solutions and gases from the East Coast accretionary prism, New Zealand. In *Isotope and geochemical techniques applied to geothermal investigations* (pp. 209–231). IAEA.
- Götze, J. (2012). Application of cathodoluminescence microscopy and spectroscopy in geosciences. *Microscopy and Microanalysis*, 18(6), 1270–1284. <https://doi.org/10.1017/S1431927612001122>
- Gurnis, M., Hall, C., & Lavier, L. (2004). Evolving force balance during incipient subduction. *Geochemistry, Geophysics, Geosystems*, 5(7). <https://doi.org/10.1029/2003GC000681>
- Hayes, G. P., Furlong, K. P., & Ammon, C. J. (2009). Intraplate deformation adjacent to the Macquarie Ridge south of New Zealand—The tectonic evolution of a complex plate boundary. *Tectonophysics*, 463(1–4), 1–14. <https://doi.org/10.1016/j.tecto.2008.09.024>

- Hayward, B. W., Black, P. M., Smith, I. E., Ballance, P. F., Itaya, T., Doi, M., et al. (2001). K-Ar ages of early Miocene arc-type volcanoes in northern New Zealand. *New Zealand Journal of Geology and Geophysics*, *44*(2), 285–311. <https://doi.org/10.1080/00288306.2001.9514939>
- Herzer, R. H., Barker, D. H. N., Roest, W. R., & Mortimer, N. (2011). Oligocene-Miocene spreading history of the northern South Fiji Basin and implications for the evolution of the New Zealand plate boundary. *Geochemistry, Geophysics, Geosystems*, *12*(2), Q02004. <https://doi.org/10.1029/2010GC003291>
- Isaac, M. J., Herzer, R. H., Brook, F. J., & Hayward, B. W. (1994). *Cretaceous and Cenozoic sedimentary basins of Northland, New Zealand*. Institute of Geological & Nuclear Sciences monograph 8. Institute of Geological & Nuclear Sciences, Lower Hutt.
- Kamp, P. J. J. (1986). The mid-Cenozoic Challenger Rift System of western New Zealand and its implications for the age of Alpine fault inception. *The Geological Society of America Bulletin*, *97*(3), 255–281. [https://doi.org/10.1130/00167606\(1986\)97<255:TMCRSO>2.0.CO;2](https://doi.org/10.1130/00167606(1986)97<255:TMCRSO>2.0.CO;2)
- Kamp, P. J. J. (1999). Tracking crustal processes by FT thermochronology in a forearc high (Hikurangi margin, New Zealand) involving Cretaceous subduction termination and mid-Cenozoic subduction initiation. *Tectonophysics*, *307*(3–4), 313–343. [https://doi.org/10.1016/S0040-1951\(99\)00102-X](https://doi.org/10.1016/S0040-1951(99)00102-X)
- Kamp, P. J. J., Tripathi, A. R. P., & Nelson, C. S. (2014). Paleogeography of late Eocene to earliest Miocene Te Kuiti Group, central-Western North Island, New Zealand. *New Zealand Journal of Geology and Geophysics*, *57*(2), 128–148. <https://doi.org/10.1080/00288306.2014.904384>
- Keller, W. R. (2005). *Cenozoic plate tectonic reconstructions and plate boundary processes in the Southwest Pacific*. PhD thesis (p. 92). California Institute of Technology. Retrieved from ProQuest Dissertations Publishing.
- Ketcham, R. A. (2005). Forward and inverse modeling of low-temperature thermochronometry data. *Reviews in Mineralogy and Geochemistry*, *58*(1), 275–314. <https://doi.org/10.2138/rmg.2005.58.11>
- Kharaka, Y. K., & Hanor, J. S. (2003). *Deep fluids in the continents. I. Sedimentary basins. Treatise on geochemistry* (Vol. 5, p. 605).
- Kiel, S., Birgel, D., Campbell, K. A., Crampton, J. S., Schiøler, P., & Peckmann, J. (2013). Cretaceous methane-seep deposits from New Zealand and their fauna. *Palaeogeography, Palaeoclimatology, Palaeoecology*, *390*, 17–34. <https://doi.org/10.1016/j.palaeo.2012.10.033>
- Kim, S. T., & O'Neil, J. R. (1997). Equilibrium and nonequilibrium oxygen isotope effects in synthetic carbonates. *Geochimica et Cosmochimica Acta*, *61*(16), 3461–3475. [https://doi.org/10.1016/S0016-7037\(97\)00169-5](https://doi.org/10.1016/S0016-7037(97)00169-5)
- King, P. R. (2000). Tectonic reconstructions of New Zealand: 40 Ma to the present. *New Zealand Journal of Geology and Geophysics*, *43*(4), 611–638. <https://doi.org/10.1080/00288306.2000.9514913>
- King, P. R., & Thrasher, G. P. (1996). *Cretaceous-Cenozoic geology and petroleum systems of the Taranaki Basin, New Zealand*. Institute of Geological & Nuclear Sciences monograph 13 (p. 244). Institute of Geological & Nuclear Sciences, Lower Hutt.
- Lamb, S. (2011). Cenozoic tectonic evolution of the New Zealand plate-boundary zone: A paleomagnetic perspective. *Tectonophysics*, *509*(3–4), 135–164. <https://doi.org/10.1016/j.tecto.2011.06.005>
- Lee, Y. J., & Morse, J. W. (1999). Calcite precipitation in synthetic veins: Implications for the time and fluid volume necessary for vein filling. *Chemical Geology*, *156*(1–4), 151–170. [https://doi.org/10.1016/S0009-2541\(98\)00183-1](https://doi.org/10.1016/S0009-2541(98)00183-1)
- Lewis, K. B., & Marshall, B. A. (1996). Seep faunas and other indicators of methane-rich dewatering on New Zealand convergent margins. *New Zealand Journal of Geology and Geophysics*, *39*(2), 181–200. <https://doi.org/10.1080/00288306.1996.9514704>
- Lloyd, S. J., Sample, J., Tripathi, R. E., Defliese, W. F., Brooks, K., Hovland, M., et al. (2016). Methane seep carbonates yield clumped isotope signatures out of equilibrium with formation temperatures. *Nature Communications*, *7*(1), 1–12. <https://doi.org/10.1038/ncomms12274>
- Ludwig, K. R. (2013). *Isoplot 4.13*. Berkeley Geochronology Center Special Publication, (Vol. 4).
- Mazengarb, C., & Harris, D. H. M. (1994). Cretaceous stratigraphic and structural relations of Raukumara Peninsula, New Zealand: Stratigraphic patterns associated with the migration of a thrust system. *Annales Tectonicae*, *8*, 100–118.
- Mazengarb, C., & Speden, I. G. (2000). *Geology of the Raukumara area, Map 6, scale 1:250 000, 1 sheet* (p. 60). Institute of Geological and Nuclear Science, Lower Hutt.
- Meyer, E. E., Quicksall, A. N., Landis, J. D., Link, P. K., & Bostick, B. C. (2012). Trace and rare Earth elemental investigation of a Sturtian cap carbonate, Pocatello, Idaho: Evidence for ocean redox conditions before and during carbonate deposition. *Precambrian Research*, *192*, 89–106. <https://doi.org/10.1016/j.precamres.2011.09.015>
- Mortimer, N. (2004). New Zealand's geological foundations. *Gondwana Research*, *7*(1), 261–272. [https://doi.org/10.1016/S1342-937X\(05\)70324-5](https://doi.org/10.1016/S1342-937X(05)70324-5)
- Mortimer, N., Herzer, R. H., Gans, P. B., Laporte-Magoni, C., Calvert, A. T., & Bosch, D. (2007). Oligocene–Miocene tectonic evolution of the South Fiji Basin and Northland Plateau, SW Pacific Ocean: Evidence from petrology and dating of dredged rocks. *Marine Geology*, *237*(1–2), 1–24. <https://doi.org/10.1016/j.margeo.2006.10.033>
- Nelson, C. S., Campbell, K. A., Nyman, S. L., Greinert, J., Francis, D. A., & Hood, S. D. (2019). Genetic link between Miocene seafloor methane seep limestones and underlying carbonate conduit concretions at Rocky Knob, Gisborne, New Zealand. *New Zealand Journal of Geology and Geophysics*, *62*(3), 318–340. <https://doi.org/10.1080/00288306.2018.1561474>
- Nelson, C. S., & Hume, T. M. (1977). Relative intensity of tectonic events revealed by the tertiary sedimentary record in the North Wanganui Basin and adjacent areas, New Zealand. *New Zealand Journal of Geology and Geophysics*, *20*(2), 369–392. <https://doi.org/10.1080/00288306.1977.10420714>
- Newman, J. (1997). New approaches to detection and correction of suppressed vitrinite reflectance. *The APPEA Journal*, *37*(1), 524–535. <https://doi.org/10.1071/AJ96031>
- Newman, J., Eckersley, K. M., Francis, D. A., & Moore, N. A. (2000). Application of vitrinite–inertinite reflectance and fluorescence (VIRF) to maturity assessment in the East Coast and Canterbury Basins of New Zealand. *New Zealand Petroleum Conference Proceedings*, *314*, 333.
- Nyman, S. L., & Nelson, C. S. (2011). The place of tubular concretions in hydrocarbon cold seep systems: Late Miocene Urenui Formation, Taranaki Basin, New Zealand. *AAPG Bulletin*, *95*(9), 1495–1524. <https://doi.org/10.1016/j.margeo.2009.03.021>
- Nyman, S. L., Nelson, C. S., & Campbell, K. A. (2010). Miocene tubular concretions in East Coast basin, New Zealand: Analogue for the subsurface plumbing of cold seeps. *Marine Geology*, *272*(1–4), 319–336. <https://doi.org/10.1016/j.margeo.2009.03.021>
- Oliver, N. H., & Bons, P. D. (2001). Mechanisms of fluid flow and fluid–rock interaction in fossil metamorphic hydrothermal systems inferred from vein–wallrock patterns, geometry and microstructure. *Geofluids*, *1*(2), 137–162. <https://doi.org/10.1046/j.1468-8123.2001.00013.x>
- Parrish, R. R., Parrish, C. M., & Lasalle, S. (2018). Vein calcite dating reveals Pyrenean orogen as cause of Paleogene deformation in southern England. *Journal of the Geological Society*, *175*(3), 425–442. <https://doi.org/10.1144/jgs2017-107>
- Paton, C., Woodhead, J. D., Hellstrom, J. C., Hergt, J. M., Greig, A., & Maas, R. (2010). Improved laser ablation U-Pb zircon geochronology through robust downhole fractionation correction. *Geochemistry, Geophysics, Geosystems*, *11*(3). <https://doi.org/10.1029/2009GC002618>
- Raine, J. I., Beu, A. G., Boyes, A. F., Campbell, H. J., Cooper, R. A., Crampton, J. S., et al. (2015). New Zealand geological timescale NZGT 2015/1. *New Zealand Journal of Geology and Geophysics*, *58*(4), 398–403. <https://doi.org/10.1080/00288306.2015.1086391>
- Rait, G. J. (1992). *Early Miocene thrust tectonics on Raukumara peninsula, Northeastern New Zealand*. PhD thesis. Victoria University of Wellington. Retrieved from Victoria University of Wellington Research Archive <http://hdl.handle.net/10063/700>

- Rait, G. J., Chanier, F., & Waters, D. W. (1991). Landward-and seaward-directed thrusting accompanying the onset of subduction beneath New Zealand. *Geology*, *19*(3), 230–233. [https://doi.org/10.1130/0091-7613\(1991\)019<0230:LASDTA>2.3.CO;2](https://doi.org/10.1130/0091-7613(1991)019<0230:LASDTA>2.3.CO;2)
- Ramsay, J. G. (1980). The crack–seal mechanism of rock deformation. *Nature*, *284*(5752), 135–139. <https://doi.org/10.1038/284135a0>
- Reyes, A. G., Christenson, B. W., & Faure, K. (2010). Sources of solutes and heat in low-enthalpy mineral waters and their relation to tectonic setting, New Zealand. *Journal of Volcanology and Geothermal Research*, *192*(3–4), 117–141. <https://doi.org/10.1016/j.jvolgeores.2010.02.015>
- Ritger, S., Carson, B., & Suess, E. (1987). Methane-derived authigenic carbonates formed by subduction-induced pore-water expulsion along the Oregon/Washington margin. *The Geological Society of America Bulletin*, *98*(2), 147–156. [https://doi.org/10.1130/0016-7606\(1987\)98<147:MACFBS>2.0.CO;2](https://doi.org/10.1130/0016-7606(1987)98<147:MACFBS>2.0.CO;2)
- Roberts, N. M., Rasbury, E. T., Parrish, R. R., Smith, C. J., Horstwood, M. S., & Condon, D. J. (2017). A calcite reference material for LA-ICP-MS U–Pb geochronology. *Geochemistry, Geophysics, Geosystems*, *18*(7), 2807–2814. <https://doi.org/10.1002/2016GC006784>
- Rowan, C. J., Roberts, A. P., & Rait, G. J. (2005). Relocation of the tectonic boundary between the Raukumara and Wairoa domains (East Coast, North Island, New Zealand): Implications for the rotation history of the Hikurangi margin. *New Zealand Journal of Geology and Geophysics*, *48*(1), 185–196. <https://doi.org/10.1080/00288306.2005.9515108>
- Saffer, D. M. (2007). 7. Pore Pressure within underthrust sediment in subduction zones. In *The seismogenic zone of subduction thrust faults* (pp. 171–209). Columbia University Press. <https://doi.org/10.7312/dixo13866-007>
- Sakai, H., Gamo, T., Ogawa, Y., & Boulegue, J. (1992). Stable isotopic ratios and origins of the carbonates associated with cold seepage at the eastern Nankai Trough. *Earth and Planetary Science Letters*, *109*(3–4), 391–404. [https://doi.org/10.1016/0012-821X\(92\)90101-Z](https://doi.org/10.1016/0012-821X(92)90101-Z)
- Sample, J. C. (1996). Isotopic evidence from authigenic carbonates for rapid upward fluid flow in accretionary wedges. *Geology*, *24*(10), 897–900. [https://doi.org/10.1130/0091-7613\(1996\)024<0897:IEFACF>2.3.CO;2](https://doi.org/10.1130/0091-7613(1996)024<0897:IEFACF>2.3.CO;2)
- Sample, J. C., Reid, M. R., Tols, H. J., & Moore, J. C. (1993). Carbonate cements indicate channeled fluid flow along a zone of vertical faults at the deformation front of the Cascadia accretionary wedge (northwest US coast). *Geology*, *21*(6), 507–510. [https://doi.org/10.1130/0091-7613\(1993\)021<0507:CCICFF>2.3.CO;2](https://doi.org/10.1130/0091-7613(1993)021<0507:CCICFF>2.3.CO;2)
- Sample, J. C., Torres, M. E., Fisher, A., Hong, W. L., Destriigneville, C., Defliese, W. F., & Tripathi, A. E. (2017). Geochemical constraints on the temperature and timing of carbonate formation and lithification in the Nankai Trough, NanTroSEIZE transect. *Geochimica et Cosmochimica Acta*, *198*, 92–114. <https://doi.org/10.1016/j.gca.2016.10.013>
- Schellart, W. P., Lister, G. S., & Toy, V. G. (2006). A Late Cretaceous and Cenozoic reconstruction of the Southwest Pacific region: Tectonics controlled by subduction and slab rollback processes. *Earth-Science Reviews*, *76*(3–4), 191–233. <https://doi.org/10.1016/j.earscirev.2006.01.002>
- Shuck, B., Gulick, S. P., Van Avendonk, H. J., Gurnis, M., Sutherland, R., Stock, J., & Hightower, E. (2022). Stress transition from horizontal to vertical forces during subduction initiation. *Nature Geoscience*, *15*(2), 149–155. <https://doi.org/10.1038/s41561-021-00880-4>
- Sibson, R. H. (1990). Conditions for fault-valve behaviour. *Geological Society, London, Special Publications*, *54*(1), 15–28. <https://doi.org/10.1144/GSL.SP.1990.054.01.02>
- Simmons, S. F., & Christenson, B. W. (1994). Origins of calcite in a boiling geothermal system. *American Journal of Science*, *294*(3), 361–400. <https://doi.org/10.2475/ajs.294.3.361>
- Stacey, J. T., & Kramers, J. S. (1975). Approximation of terrestrial lead isotope evolution by a two-stage model. *Earth and Planetary Science Letters*, *26*(2), 207–221. [https://doi.org/10.1016/0012-821X\(75\)90088-6](https://doi.org/10.1016/0012-821X(75)90088-6)
- Stagpoole, V., & Nicol, A. (2008). Regional structure and kinematic history of a large subduction back thrust: Taranaki Fault, New Zealand. *Journal of Geophysical Research*, *113*(B1), B01403. <https://doi.org/10.1029/2007JB005170>
- Stoneley, R. (1968). A lower tertiary decollement on the East Coast, North Island, New Zealand. *New Zealand Journal of Geology and Geophysics*, *11*(1), 128–156. <https://doi.org/10.1080/00288306.1968.10423680>
- Strogen, D. P., Higgs, K. E., Griffin, A. G., & Morgans, H. E. (2019). Late Eocene–early Miocene facies and stratigraphic development, Taranaki Basin, New Zealand: The transition to plate boundary tectonics during regional transgression. *Geological Magazine*, *156*(10), 1751–1770. <https://doi.org/10.1017/S0016756818000997>
- Taylor, S. R., & McLennan, S. M. (1985). *The continental crust: Its composition and evolution* (p. 312). Blackwell.
- Tera, F., & Wasserburg, G. J. (1972). U–Th–Pb systematics in three Apollo 14 basalts and the problem of initial Pb in lunar rocks. *Earth and Planetary Science Letters*, *14*(3), 281–304. [https://doi.org/10.1016/0012-821X\(72\)90128-8](https://doi.org/10.1016/0012-821X(72)90128-8)
- Tostevin, R., Shields, G. A., Tarbuck, G. M., He, T., Clarkson, M. O., & Wood, R. A. (2016). Effective use of cerium anomalies as a redox proxy in carbonate-dominated marine settings. *Chemical Geology*, *438*, 146–162. <https://doi.org/10.1016/j.chemgeo.2016.06.027>
- Toth, J., & Gurnis, M. (1998). Dynamics of subduction initiation at preexisting fault zones. *Journal of Geophysical Research*, *103*(B8), 18053–18067. <https://doi.org/10.1029/98jb01076>
- Uysal, I. T., Feng, Y. X., Zhao, J. X., Bolhar, R., Işik, V., Baublys, K. A., et al. (2011). Seismic cycles recorded in late Quaternary calcite veins: Geochronological, geochemical and microstructural evidence. *Earth and Planetary Science Letters*, *303*(1–2), 84–96. <https://doi.org/10.1016/j.epsl.2010.12.039>
- Van de Lagemaat, S. H. A., Mering, J. A., & Kamp, P. J. J. (2021). LA-ICP-MS and stable isotope data of Waihou Bay (North Island, New Zealand) carbonate veins [Dataset]. Mendeley Data, V1. <https://doi.org/10.17632/tjhzpdkvmp.1>
- Van de Lagemaat, S. H. A., Van Hinsbergen, D. J. J., Boschman, L. M., Kamp, P. J. J., & Spakman, W. (2018). Southwest Pacific absolute plate kinematic reconstruction reveals major Cenozoic Tonga-Kermadec slab dragging. *Tectonics*, *37*(8), 2647–2674. <https://doi.org/10.1029/2017TC004901>
- Vrolijk, P., & Sheppard, S. M. (1991). Syntectonic carbonate veins from the Barbados accretionary prism (ODP Leg 110): Record of palaeohydrology. *Sedimentology*, *38*(4), 671–690. <https://doi.org/10.1111/j.1365-3091.1991.tb01014.x>
- Wagner, T., Magill, C. R., & Herrle, J. O. (2018). Carbon isotopes. In W. M. White (Ed.), *Encyclopedia of geochemistry. Encyclopedia of earth sciences series*. Springer. https://doi.org/10.1007/978-3-319-39312-4_176
- Walcott, R. I., Christoffel, D. A., & Mumme, T. C. (1981). Bending within the axial tectonic belt of New Zealand in the last 9 Myr from paleomagnetic data. *Earth and Planetary Science Letters*, *52*(2), 427–434. [https://doi.org/10.1016/0012-821X\(81\)90195-3](https://doi.org/10.1016/0012-821X(81)90195-3)
- Weissel, J. K., Hayes, D. E., & Herron, E. M. (1977). Plate tectonic synthesis: The displacements between Australia, New Zealand and Antarctica since the Late Cretaceous. *Marine Geology*, *25*(1–3), 231–227. [https://doi.org/10.1016/0025-3227\(77\)90054-8](https://doi.org/10.1016/0025-3227(77)90054-8)

References From the Supporting Information

- Mering, J. A., & Barker, S. L. (2018). Precise measurement of the hydrogen isotope composition of phyllosilicates by continuous flow off-axis integrated cavity output spectroscopy. *Analytical Chemistry*, *90*(4), 2852–2859. <https://doi.org/10.1021/acs.analchem.7b04992>

Petrus, J. A., & Kamber, B. S. (2012). VizualAge: A novel approach to laser ablation ICP-MS U-Pb geochronology data reduction. *Geostandards and Geoanalytical Research*, 36(3), 247–270. <https://doi.org/10.1111/j.1751-908X.2012.00158.x>